TiO2 as a Photocatalyst for Water Splitting—An Experimental and Theoretical Review

Håkon Eidsvåg [1,*] , **Said Bentouba** [1] , **Ponniah Vajeeston** [2] , **Shivatharsiny Yohi** [3] and **Dhayalan Velauthapillai** [1,*]

1 Department of Computing, Mathematics and Physics, Western Norway University of Applied Sciences, Inndalsveien 28, Box 5063, N-5009 Bergen, Norway; Said.Bentouba@hvl.no

2 Center for Materials Science and Nanotechnology, Department of Chemistry, University of Oslo, Box 1033 Blindern, N-0315 Oslo, Norway; ponniah.vajeeston@smn.uio.no

3 Department of Chemistry, Faculty of Science, University of Jaffna, Sir. Pon, Ramanathan Rd, Jaffna 40000, Sri Lanka; srtharsha12@gmail.com

* Correspondence: heid@hvl.no (H.E.); dhayalan.velauthapillai@hvl.no (D.V.); Tel.: +47-980-61-444 (H.E.); +47-55-58-77-11 (D.V.)

Abstract: Hydrogen produced from water using photocatalysts driven by sunlight is a sustainable way to overcome the intermittency issues of solar power and provide a green alternative to fossil fuels. TiO2 has been used as a photocatalyst since the 1970s due to its low cost, earth abundance, and stability. There has been a wide range of research activities in order to enhance the use of TiO2 as a photocatalyst using dopants, modifying the surface, or depositing noble metals. However, the issues such as wide bandgap, high electron-hole recombination time, and a large overpotential for the hydrogen evolution reaction (HER) persist as a challenge. Here, we review state-of-the-art experimental and theoretical research on TiO2 based photocatalysts and identify challenges that have to be focused on to drive the field further. We conclude with a discussion of four challenges for TiO2 photocatalysts—non-standardized presentation of results, bandgap in the ultraviolet (UV) region, lack of collaboration between experimental and theoretical work, and lack of large/small scale production facilities. We also highlight the importance of combining computational modeling with experimental work to make further advances in this exciting field.

Keywords: TiO2; water-splitting; theoretical; experimental; DFT

1. Introduction

Over the last years, there has been a steadily increasing focus on clean, renewable energy sources as a priority to hinder the irreversible climate change the world is facing and to meet the continuously growing energy demand [1]. One hour of solar energy can satisfy the energy consumption of the whole world for a year [2]. Hence, direct harvesting of solar light and its conversion into electrical energy with photovoltaic cells or chemical energy by photoelectrochemical reactions are the most relevant technologies to overcome this challenge. Conventionally, both technologies rely on the collection of light in semiconductor materials with appropriate bandgaps matching the solar spectrum, and thus providing a high-energy conversion efficiency.

Unfortunately, the technology has drawbacks, which prevent it from overtaking non-renewable energy as the main energy source. A major issue is the uneven power distribution caused by varying solar radiation and a lack of proper storage alternatives. As a solution to this problem, the focus is moving toward research on storage options for the produced electricity, which we can divide into mechanical and electrochemical storage systems. For example, in Oceania, pumped hydroelectricity (mechanical) is the most common storage system for excess electricity [3]. Different batteries (lithium–ion, sodium–sulfur (S), vanadium, etc.), hydrogen fuel cells, and supercapacitors are the current

focus areas for electrochemical storage [3]. There are several reasons for choosing hydrogen as a way to store solar energy, namely, (1) there is a high abundance of hydrogen from renewable sources; (2) it is eco-friendly when used; (3) hydrogen has a high-energy yield, and (4) it is easy to store as either a gas or a liquid [4–6].

The high energy yield and ease of storage make hydrogen viable as fuel for the long transport sector; airplanes, cruise ships, trailers, and cargo ships [7,8]. The realization of a green energy shipping fleet could alone yearly cut 2.5% of global greenhouse emissions (GHG) [9]. However, to succeed in this strategy, hydrogen must be produced in a clean and renewable way.

As water splitting got the attention of the researchers in the 1970s, titanium dioxide became the most prominent photocatalyst used [10]. There are several good reasons for this: low cost, chemical stability, earth abundance, and nontoxicity [11]. However, TiO_2 also sports a wide bandgap (3.0–3.2 eV), which reduces the potential for absorption of visible light [11]. Due to TiO_2s structural and chemical properties, it is possible to engineer the bandgap, light absorption properties, recombination time, etc. by increasing the active sites and improving the electrical conductivity [12]. TiO_2 exists in several different polymorphs that all behave differently. The most common ones are rutile, brookite, and anatase as shown in Figure 1. Rutile and anatase TiO_2 are the most used polymorphs for photocatalytic water splitting; nevertheless, some attempts with amorphous TiO_2 ($aTiO_2$) have been made as shown in Figure 2.
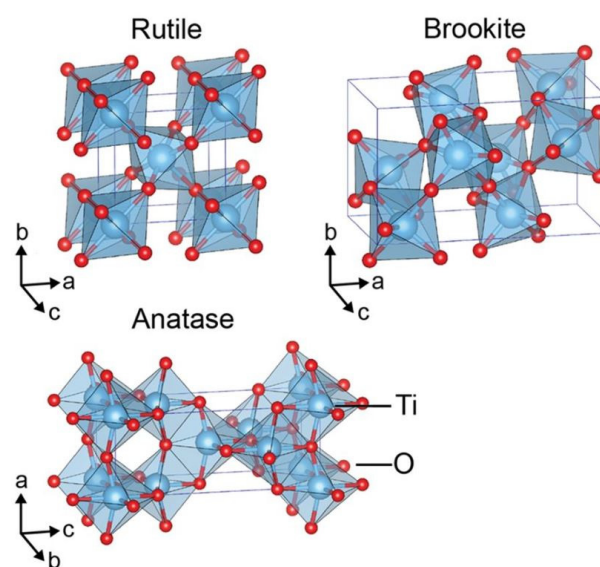
Figure 1. Crystal structures of TiO_2 rutile (tetragonal, P42/mmm), brookite (orthorhombic, Pbca), and anatase (tetragonal, I41/amd) polymorphs. Reused with permission from [13].
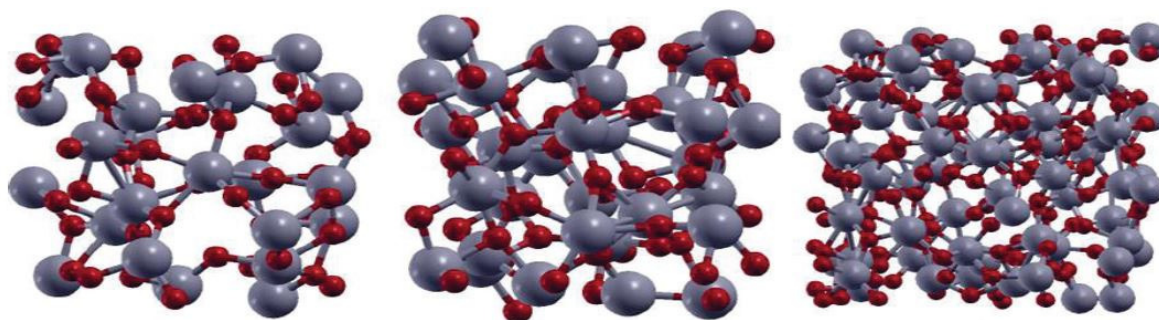

Figure 2. The structure of 72-atom (**left**), 96-atom (**middle**), and 216-atoms (**right**) models of amorphous TiO_2. The red and grey spheres represent O and Ti atoms respectively. Reused with permission from [14]. Copyright 2012, with permission from Elsevier.

Several attempts have been made to introduce dopants to improve the optical absorption of TiO_2. For example, Zhang et al. found that 12.5% copper (Cu)-doped anatase TiO_2 showed a broader absorption peak than pure anatase titanium dioxide [15]. Through a theoretical study, they found that Cu introduces an unoccupied impurity continuum band at the top of the valence band, which explains the improved optical absorption. Another theoretical study, conducted by Morgade and Cabeza in 2017, shows that co-doping of TiO_2 with (Pt, V) and (C, N) narrows the bandgap and favorably modifies the position of the valence and conduction band edges [16]. Our study will provide an insight into current theoretical and computational studies carried out on water splitting using either pure or doped TiO_2 semiconductors. In addition, we will compare it with the state of art experimental studies conducted within the field. Our aim is to help bridge the gap between theoretical simulations and experimental research. The two approaches complement each other and when combined could support the field moving forward toward the realization of the hydrogen economy. The theoretical study allows testing of the properties of thousands of different materials with different parameters to gain an understanding of how and why certain dopants and material combinations work. However, the computational models are worked out using perturbation theory, which lowers the overall accuracy of the results. At the same time, an experimental study is important to verify the theoretical results and find the best methods to synthesize the materials in practice.

2. Solar-Driven Hydrogen Production

Most of the commercial production of hydrogen stems from four sources: natural gas, coal, oil, and electrolysis. Of these, steam reforming alone stands for 48% of the world's hydrogen production, while coal contributes 18%, oil 30%, and electrolysis 4% [17]. The first three hydrogen production processes are energy-consuming and use non-renewable energy sources, which is unattractive for environment protection and climate change [18,19]. However, the production of hydrogen by electrolysis requires only water and electrical current. To have green hydrogen, produced friendly to the environment, we propose to use renewable energy sources—wind, hydro, and solar power—to produce the electric current needed for the electrolysis of water. Solar power is ideal due to the high amount of incoming energy. There are several functional methods used in driving the electrolysis process, i.e., thermochemical water splitting [20], photo-biological water splitting [21], and photocatalytic water splitting [22]. Furthermore, photocatalytic water splitting (PWS) is considered the best option, due to the following reasons: (1) PWS has a good solar-hydrogen conversion efficiency, (2) it has a low production cost, (3) oxygen and hydrogen can easily be separated during the PWS process, and (4) hydrogen electrolysis could be used on both small- and large-scale facilities [4,22,23].

2.1. Photocatalytic Water Splitting (PWS)

The photocatalytic process splits water (H_2O) into hydrogen (H_2) and oxygen (O_2) in the presence of a catalyst and natural light; it is an artificial photosynthesis method. Figure 3 shows a schematic illustration of the major steps involved in the process of photocatalytic water splitting. In the first step (1), electron–hole pairs are generated in the presence of irradiation. This is carried out by utilizing the semiconducting nature of the photocatalyst to excite electrons from the valence band (VB) to the conduction band (CB). Photons with energies larger than the bandgap can excite electrons from the VB to the CB. The second step (2) consists of charge separation and migration of the photogenerated electron-hole pairs. Ideally, all electrons and holes reach the surface without recombination to maximize the efficiency of the photocatalyst. In the final step (3), the electrons, which move from the CB to the surface of the catalyst participate in a reduction reaction and generate hydrogen, and the holes diffuse from the VB to the surface of the photocatalyst involved in an oxidation reaction to form oxygen. In general, the efficiency of the catalyst can be enhanced by including dopants or co-catalysts that include metals or metal oxides, such as Pt, NiO, and RuO_2, which can act as the active sites via enhancing electron mobility.

The redox and oxidations reactions on the surface of the photocatalyst are described by the following equations [24]:
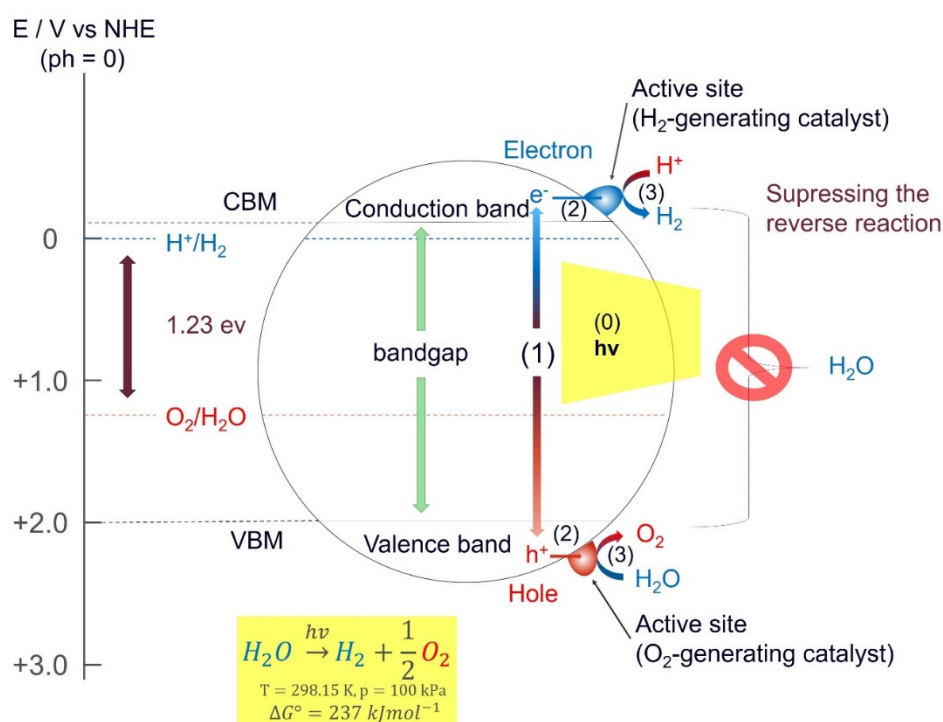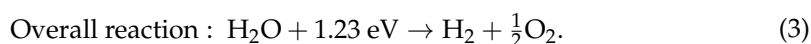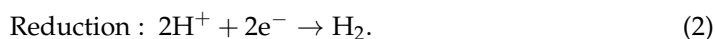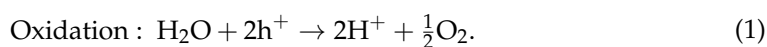
$$\text{Oxidation}: \ H_2O + 2h^+ \rightarrow 2H^+ + \tfrac{1}{2}O_2. \tag{1}$$

$$\text{Reduction}: \ 2H^+ + 2e^- \rightarrow H_2. \tag{2}$$

$$\text{Overall reaction}: \ H_2O + 1.23 \ eV \rightarrow H_2 + \tfrac{1}{2}O_2. \tag{3}$$

Figure 3. Schematic illustration of the main photocatalytic steps for a semiconductor photocatalyst: (1) light is absorbed to generate electron–hole pairs; (2) migration of excited carriers (electrons and holes) to the surface; (3) surface reaction to produce hydrogen with electrons and oxygen with holes. Reproduced with permission from [25], Copyright 2013, with permission from Elsevier.

The process of water splitting is highly endothermic and requires a Gibbs free energy of 1.23 eV per electron, which corresponds to light with a wavelength of 1008 nm. This means that the photocatalyst must have a bandgap > 1.23 eV, or else the electrons will not have enough energy to start the reaction. In practice, this limit should be 1.6 eV to 1.8 eV due to some overpotentials [24]. Naturally, it should not be too high either, as that would reduce the amount of visible light the photocatalyst can absorb. This means that it is important to find suitable catalysts with a bandgap between 1.6–2.2 eV to ensure maximum absorption of the incoming light. Another important factor regarding the efficiency of a photocatalyst is the recombination time, i.e., the time it takes for an electron to recombine with a hole. If recombination occurs before the electrons can reach the surface and interact with the water molecules, the energy gets wasted and no redox reaction takes place. Unfortunately, there are only a few materials with sufficient recombination time and a satisfactory bandgap that have been identified. However, a recent study by Takata et. al. demonstrates that it is possible to achieve water splitting without any charge recombination losses [26]. With $SrTiO_3$ as the photocatalyst loaded with Rh, Cr, and Co as cocatalysts, they achieved an external quantum efficiency up to 96% at wavelengths between 350 nm and 360 nm [26]. This is equivalent to having an internal quantum efficiency of almost

unity. The requirements for having an efficient photocatalyst can be summarized in the solar–hydrogen conversion efficiency (STH) equation [27] as follows:

$$\eta_{STH} = \eta_A \times \eta_{CS} \times \eta_{CT} \times \eta_{CR}. \tag{4}$$

The STH conversion efficiency depends on (1) the efficiencies of light absorption (η_A), (2) charge separation (η_{CS}), (3) charge transport (η_{CT}), and (4) charge collection/reaction efficiency (η_{CR}). The efficiency of the photocatalyst depends on several factors and they are elaborated in the following section.

2.2. Important Aspects of Photocatalytic Efficiency for Nanomaterials

There are several ways to improve and modify the fundamental properties of a photocatalyst by focusing on its shape, size, order, uniformity, and morphology.

2.2.1. Crystallinity

Research has shown that the crystallinity of the material affects its optoelectronic properties [28,29]. Structures with a high crystallinity perform better than amorphous variations of the same material. The increase in crystallinity reduces the number of defects in the structures and thus decreases the electron-hole recombination sites, which leads to a better catalytic activity [30–33]. Liu et al. studied the effect of crystalline TiO_2 nanotubes against that of amorphous TiO_2 nanotubes and found that better photocurrent properties were attained with the crystalline structures due to the lower amount of electron-hole recombination [34]. In another study, enhanced hydrogen production was obtained using extremely ordered nanotubular TiO_2 arrays [35].

2.2.2. Dimensionality

Nanomaterials can be classified into four different categories depending on their dimensionality—zero-dimensional (0D), one-dimensional (1D), two-dimensional (2D), and three-dimensional (3D) [36,37]. Zero-dimensional (0D) nanostructures used in PWS are primarily quantum dots (QDs) and hollow shells. In general, QDs are used to decorate the photocatalyst because they increase the visible light absorption and reduce the electron-hole recombination [38–40]. One-dimensional (1D) structures include nanorods, nanotubes, and nanowires, which are all attractive for photocatalysts. It is found that nanorod and nanowire arrays result in a more efficient photogenerated electron transport and collection [41–43]. On the other hand, nanotubes have a higher surface area for redox reactions compared to nanorods or nanowires although they have less material for light absorption [44,45]. Two-dimensional (2D) nanostructures have a high surface area and a small thickness that reduces the travel distance for generated holes. This results in efficient light harvesting. Lastly, 3D nanostructures are promising candidates for PWS because they can be designed into high-performance photoanodes [27]. In general, it is possible to design and create nanostructures that cater to specific tasks.

2.2.3. Temperature and Pressure

Temperature and pressure during the production phase will affect the resulting properties of a photocatalyst. Research shows that by varying the pressure, the STH performance of the catalyst will change [46]. Another research group found that by using a low-temperature thermal treatment process the charge transfer resistance could be reduced [47].

2.2.4. Size

As mentioned TiO_2 exist in three phases, anatase (tetragonal; a = 3.7845 Å; c = 9.5143 Å), rutile (tetragonal; a = 4.5937 Å; c = 2.9587 Å), and brookite (orthorhombic; a = 5.4558 Å; b = 9.1819 Å; c = 5.1429 Å). Among the three different crystalline phases of TiO_2, anatase exhibits the highest stability for particle size less than 11 nm, whereas rutile shows thermodynamic stability for particle size greater than 35 nm, and brookite is stable in the size range

of 11–35 nm. The size of the nanomaterials and cocatalyst can alter the overall performance of the system. Smaller particles are dominated by electrokinetics and are thus more suited for photocatalysis. Alternatively, larger particles are better suited for photoelectrochemical (PEC) water splitting because they have a lower electron–hole recombination rate [48]. The size of the particles also influences the electron-hole recombination time. In larger particles the travel distance to the active sites on the surface becomes longer, thus increasing the probability for electron-hole recombination. This probability is decreased in smaller particles due to the shorter migration distance [49,50].

2.2.5. Bandgap

The bandgap is one of the most important properties of the photocatalyst. It is defined as the energy needed for an electron to move from the valence band maximum (VBM) to the conduction band minimum (CBM) in a semiconductor. In addition to a fitting bandgap, the CBM must be more negative than the redox potential of H^+/H_2 (0 V vs. normal hydrogen electrode (NHE)), while the VBM must be more positive than the redox potential of O_2/H_2O (1.23 V). Therefore, the theoretical minimum bandgap for water splitting is 1.23 eV. Nanomaterials are used to tune the band positions and the bandgap toward the appropriate range of 1.6 eV to 2.2 eV [51–53].

2.2.6. pH Dependency

The pH value of the solution in which the photocatalyst is placed affects the end STH efficiency [54]. It will similarly affect the stability and lifetime of the catalyst. Photoelectrochemical water splitting is very dependent on the pH of the electrolyte solution, which determines the net total charge adsorbed at the surface of the catalyst. The migration of ions during the reactions may weaken the surface of the electrode. The electrode incorporated with nanomaterials exhibits better stability in different pH conditions, however, it was evident that the stability was further improved when the solution is buffered [55–57].

2.2.7. Light

It is important that the light source be specified, as semiconductors doped with nanomaterials can absorb both infrared and UV light in addition to visible light [58].

2.3. Theoretical Methods

Numerical studies of electronic, optical and mechanical characterization of TiO_2 polymorphs are performed as ab initio calculations within the framework of density functional theory (DFT). However, the calculation model and details vary between the researchers depending on the calculation tool/code chosen; for example, Vienna ab initio simulation package (VASP) [59–64], CASTEP [65], CRYSTAL [66,67], and GPAW [68]. In general, the interaction between the core and the valence electrons is described by the projector augmented-wave method [69,70]. The electron properties are calculated by G_0W_0 [71,72], HSE06 [73,74], or by the generalized gradient approximation (GGA, which is less accurate but faster) [75]. It is possible to calculate the stress tensor by applying a set of strains to the crystal, which leads to the elastic constants (e.g., VASPKIT [76]). Moreover, it is possible to calculate the real space force constants of the supercell, and then to evaluate this with appropriate software (e.g., Phonopy [77]) in order to find the phonon frequencies for dynamical stability, heat capacity, free energy, and entropy analysis.

2.4. Experimental Methods

Several synthesis methods are used for the synthesis of TiO_2 materials depending on the end application and experiment performed. The methods can roughly be divided into thermal reactions, deposition methods, sol–gel, Micelle, and electromagnetic methods. In general, the thermal methods are heterogeneous reactions in the presence of aqueous solvents or mineralizers under high pressure and temperature [78–80]. Deposition methods (e.g., chemical vapor deposition and electrodeposition) are primarily used to create thin-

film materials or coatings on a substrate [81–83]. Sol–gel methods utilize the conversion of a liquid solution (sol) into a solid gel phase, in which the nanoparticles are formed by hydrolysis and condensation [78,84]. Micelles are the long-chain molecules made by surfactants, which contain a hydrophilic head and a hydrophobic chain. Self-assembling of these amphiphilic molecules forms an organized structure in solution [85]. The ultrasound technique can be used for preparations of a wide range of nanomaterials, especially high-surface-area transition metals, carbides, oxides, alloys, and colloids [84,86]. However, if the goal is to create a dielectric material, then the microwave method can be used [78,87].

3. Theoretical Research

The amount of theoretical and computational research has increased over the last years due to improved accuracy of the models and increased computing power. As with experimental work, most of the focus is on various dopants for TiO_2. The majority of research is conducted on anatase because that phase seems most promising for water splitting. However, rutile TiO_2 does have some interesting properties.

3.1. Metal Dopants

A large part of the conducted research is devoted to metal dopants and their contribution to a broadened bandgap of photocatalyst TiO_2. In a comprehensive study, Pan et al. investigated how noble metals could enhance the catalytic activity of anatase TiO_2 for hydrogen evolution reaction [88]. They proposed three different structural models for hydrogenated anatase TiO_2, as seen in Figure 4, and proposed the preferred location (H1 in Figure 4a) of the hydrogen atom when TiO_2 was noble metal doped. This is because of the strongly localized hybridization between hydrogen and TiO_2 [88]. Based on these findings, they showed that anatase TiO_2 was easy to hydrogenate, and the introduced hydrogen could improve the electronic transport between the conduction band and valence band near the Fermi level [88]. In general, silver (Ag)- and gold (Au)-doping are more thermodynamically stable than that of platinum (Pt)-, palladium (Pd)- and ruthenium (Ru)-doping. The band structures for noble metal-doped TiO_2 are shown in Figure 5, and it is clearly seen that the introduction of dopants reduces the bandgap of TiO_2. However, Ag-doping seems to be the best option for noble metal doping of TiO_2 as the other dopants reduce the bandgap below 1.23 eV [88].
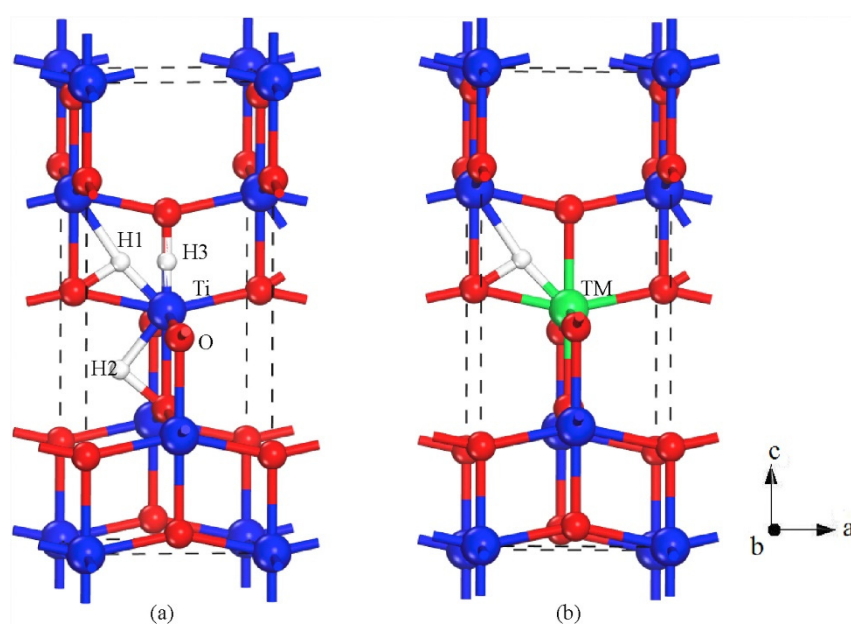

Figure 4. Structural model for (**a**) possible locations of H dopants and (**b**) hydrogenated noble-metal doped TiO_2. Reprinted with permission from [88]. Copyright 2018, with permission from Elsevier.
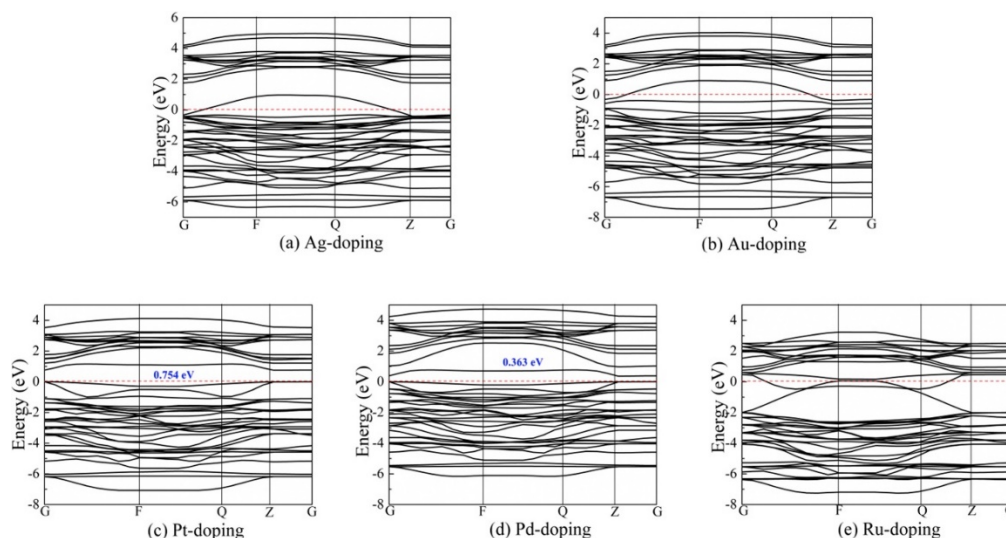
Figure 5. Calculated band structure, using generalized gradient approximation (GGA) with Perdew-Burke-Ernzerhof (PBE) exchange-energy, in the Brillouin zone for, (**a**) Ag-doping, (**b**) Au-doping, (**c**) Pt-doping, (**d**) Pd-doping, and (**e**) Ru-doping. Reprinted with permission from [88]. Copyright 2018, with permission from Elsevier.

Y. Zhang et al. doped (001) anatase TiO_2 with Pt, cobalt (Co), and Ru [89], which led to surface-localized states that enhanced the electron transfer at the surface. However, another study by S.T Zhang et al. showed that to achieve a stable interface between supported Ru_n (n = 1–10, 20, 22) clusters and TiO_2, $n > 6$ was needed [90]. Interestingly enough, this is among the preferred geometries for TiO_2 [90].

Metal dopants decrease the bandgap, and as shown by Jin et al., Pt, Pd, rhodium (Rh), and Ru single atom doping significantly reduces the work function of the compound [91].

Another option to increase the optical absorption is to use iron (Fe) or nickel (Ni) as dopants because they will induce impurity states in the forbidden region [92]. Electrons with energy less than the bandgap can use these impurity states as steps when moving from the valence band to the conduction band. Especially co-doping of TiO_2 with Fe and Ni results in higher absorption and reduced electron–hole recombination according to Lin et al. [92]. Ghuman et al. also showed that Fe^{2+} doped $aTiO_2$ adsorbs water better than pristine $aTiO_2$ and that it also has a better photocatalytic effect [93].

Introducing Cu and/or N dopants will also create isolated states in the bandgap, and therefore, TiO_2 doped with these dopants function better than pure anatase TiO_2 [94]. Assadi et al. showed that the improved photocatalytic activity in Cu/TiO_2 was because of effective bandgap narrowing and increased charge transfer (electronic interactions) and not surface chemistry [95]. Wei Zhang et al. found that the stability of Cu doped TiO_2 depends on which oxygen atoms that is replaced with Cu atoms. [15] They observed a blueshift in absorption for anatase TiO_2 (101) compared to bulk TiO_2, while in Cu-doped bulk anatase TiO_2 they observed a redshift in optical absorption [15]. Co-doped $SrTiO_3$ has a narrower bandgap compared to that of pure TiO_2 according to Sikam et al. and this is due to states being formed in the gap [96]. In addition, they also found that co-doping resulted in magnetism due to inequality of spin down and spin up states [96]. Ghuman et al. looked into the difference between monodoping and co-doping using nitrogen (N) and niobium (Nb) on amorphous TiO_2 [97]. They found that monodoping reduces the bandgap but it also increases the number of recombination centers [97]. Charge compensated co-doping, on the other hand, reduces the bandgap with 0.4 eV and suppresses the recombination effect by eliminating band gap states [97]. S and Nb co-doping of anatase TiO_2 resulted in a bandgap of 2.15 eV as shown by Ren et al. [98].

However, not all states in the bandgap are appreciated; Gao et al. looked into how Mg doping could reduce the shallow defect states under the CBM in TiO_2, increasing the photocatalytic effect [99].

Although several different dopants have been proposed and tested, not all of them are viable to be incorporated into TiO_2. Chen et al. used cerium (Ce), praseodymium (Pr), europium (Eu), and gadolinium (Gd) dopants to see how they would incorporate with TiO_2 [100]. They found that Ce was the easiest among these, while Pr and Gd had low substitutional energy and should be able to be incorporated into TiO_2 [100]. Eu on the other hand was difficult to incorporate with TiO_2 [100]. Ce, Pr, and Eu monodoping should move the light absorption more toward/into the visible light region [100]. Another approach when using lanthanides could be ion triple doping as showcased by Li et al. [101]. Through co- and triple-doping they improved the oxidizing ability, light absorption, and charge carrier separation of their photocatalyst (Bi_2MoO_6) [101].

3.2. Non-Metal Dopants

In an attempt to find non-metal dopant alternatives Shi et al. co-doped anatase TiO_2 with C and neodymium (Nd) and found tuned band gaps, which were lower than that of pure TiO_2: C@O and Nd@Ti, 2.372 Ev, and carbon (C) and Nd @ TiO_2, 2.850 eV [102]. The main function of the C and Nd dopants is to enhance the intensity of light absorption and to extend the optical absorption range into the visible light region respectively. This is clearly seen from Figure 6, in which the optical absorption spectra of TiO_2 do not extend into the visible light region, while both C doping and C and Nd doping extend the absorption range into the visible light region and effectively enhancing the efficiency of the photocatalysts. Experimental studies shown in Figure 6c confirmed these findings. By using graphite carbon spheres on TiO_2 Jiang et al. introduced isolated energy levels between the VBM and the CBM [103]. These intermediate bandgaps increase the number of electrons that could be excited from the VB to the CB.

Gurkan et al. found that selenium (Se) doping introduces localized mid-gap levels that increase the visible light photocatalytic effect [104]. However, no significant change in the position of the band edges was observed. A study by Zhao et al. showed that N, Co, Co–N, Co–2N, and Co–3N dopants all increased the optical absorption rate compared to that of undoped TiO_2 [105]. Unfortunately, Co–N and Co–3N shift the CBM below the H^+/H_2 reduction potential, which means that it is not useful for water splitting [105]. Pengfei Wang et al. revealed that carbonate could be incorporated into mesoporous TiO_2 and significantly improve the visible light hydrogen evolution [106]. In addition, the intimate homo-junctions between anatase and rutile phases and graphite carbon on the surface of TiO_2 can significantly help promote the separation of charge carriers [106].
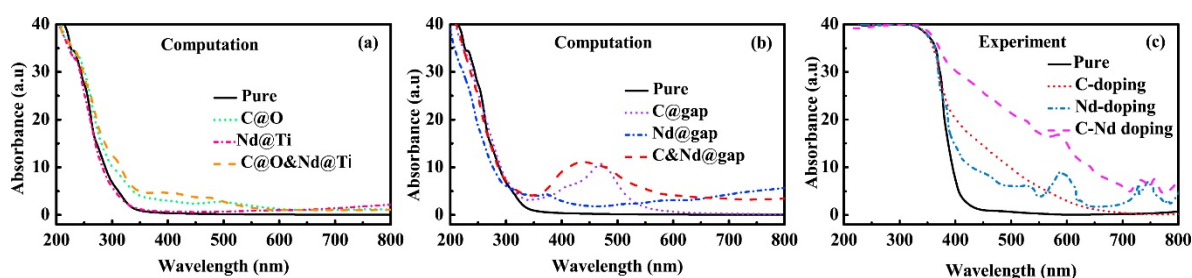
Figure 6. Theoretical and experimental optical absorption spectra for pure and doped TiO_2 structures. (**a**) Computational obtained spectra for substitutional doping, (**b**) computational obtained spectra for TiO_2 doped with the dopants at different interstitial sites, and (**c**) experimental obtained optical absorption spectra for C, Nd, and C+Nd doped TiO_2 from [107]. Reprinted with permission from [102]. Copyright 2017, with permission from Elsevier.

In an attempt to decrease the bandgap of TiO_2, Zongyan et al. used boron (B), C, N, fluorine (F), phosphorus (P), S, and chlorine (Cl) as dopants on anatase TiO_2 [108]. The tuned bandgaps for TiO_2 with the dopants (B, C, N, P and S) were 2.72 eV, 2.44 eV, 2.74 eV, 2.38 eV, and 2.59 eV, respectively [108]. The improvements are due to new impurity energy levels, which red-shift their fundamental absorption edges to the visible light region [108].

In addition, they found that higher dipole moments could lead to easier separation of the photoexcited electron-hole pairs, which would increase the photocatalytic effect [108].

There has been some research on TiO_2/g–C_3N_4 heterostructure photocatalysts. For example, Yali Zhao et al. co-doped TiO_2/g–C_3N_4 with Cu and N [109]. This resulted in an obvious narrowing of the bandgap compared with pure TiO_2, co-doping induces impurity states of N 2p and hybridized states of Cu 3d and N 2p in the bandgap of TiO_2/g–C_3N_4 [109]. Yanming Lin et al. used TiO_2/g–C_3N_4 heterostructure through interfacial coupling for H_2 production. The calculated band gap was significantly reduced compared to pure TiO_2 [110]. TiO_2/g–C_3N_4 heterostructure also has a higher CBM energy, which provides the photoexcited electrons with stronger reducing power to produce more hydrogen per unit time compared with TiO_2 [110].

3.3. Rutile

Although most researchers focus on anatase TiO_2, there has been some development on rutile TiO_2 as well. Atanelov et al. doped rutile TiO_2 with C and it seems to have worse photocatalytic performances than pure TiO_2, this is due to C–O dimes creating mid-band states [111]. However, N doped rutile TiO_2 introduced no mid-bandgap states [111]. Ghuman et al. used Rh to dope rutile TiO_2 and found that it had a lower bandgap but with more recombination centers [112]. By using Rh–Nb (charge compensated doping) as co-dopants on rutile TiO_2, they obtained no isolated bandgap states that might act as a recombination center [112]. Moreover, the bandgap was decreased by 0.5 eV, which makes it a better photocatalyst [112].

3.4. Nanotubes

Research on different TiO_2 nanostructures has led to some interesting results. Lisovski et al. doped TiO_2 nanotubes with sulfur and achieved a narrower bandgap compared to that of pure TiO_2 [113]. The band edges were also close to the limits for efficient water splitting [113]. In another article, Lisovski et al. present nitrogen (N), S, and S-and-N doping of six-layer (101) anatase TiO_2 nanotubes [114]. They found that monodoping with N or S reduces the photocatalytic effect of the nanotubes [114]. However, co-doping with N and S could improve the photocatalytic activity, although it depends on the defect concentration [114]. Dmitry Bocharov et al. used TiO_2 (4,4) nanotubes doped with scandium (Sc), depicted in Figure 7, and found that they were a good candidate with a bandgap of 1.8–1.9 eV [115]. Working on the same variation of nanotubes, E.P. D'yachkov et al. found that doping with Nb, molybdenum (Mo), technetium (Tc), and Pd leads to bandgaps around 2 eV [116]. This is a significant decrease from around 4 eV for undoped (4,4) TiO_2 nanotubes [116]. Lisovski et al. also investigated if the arrangement of bandgap edges would change when going from bulk to nanotubes. They found that this only happened if the diameter of the nanotubes was small, i.e., the internal strain was extremely large [117].
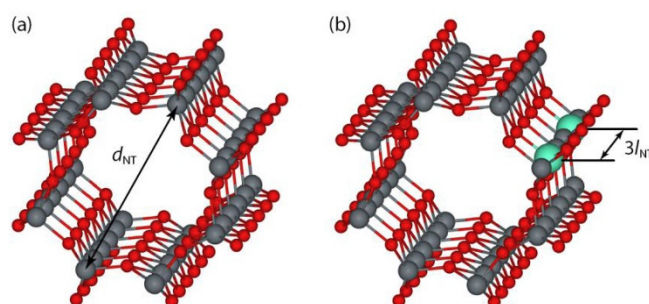
Figure 7. Structural models of non-optimized (**a**) pristine and (**b**) doped armchair type (4,4) fluorite-structured TiO_2 nanotubes. The red balls represent O, grey balls are TiO_2, and the turquoise balls represent the 3d-metal dopants substituted for Ti atoms. The nanotube diameter (d_{nt}) is 0.84 nm and the dopant concentration is considered to be 4.17%. Reprinted with permission from [115]. Copyright 2017, with permission from Elsevier.

3.5. Pure TiO2

Naturally, some focus had been on pure TiO_2 and its different states, looking into which one was most suited for photocatalytic activity.

Ma et al. found that the (101) facet had higher activity compared to other facets of TiO_2 [118], which was an important breakthrough. If we have pristine conditions and water molecules, water splitting can be expected both with rutile and anatase TiO_2 according to Deak et al. [119]. This is generally not the case because the surface will contain bridging OH^+ and the terminal OH^- (dissociated water). In these conditions, anatase TiO_2 is the best for water splitting [119]. However, by increasing the OH^+/OH^- ratio, one can increase the driving force for water splitting [119]. Hanaor et al. [120] looked into the phase stability of anatase and rutile TiO_2, with and without doping. Pure TiO_2 has a more stable rutile phase than anatase and the transformation from anatase TiO_2 to rutile TiO_2 is irreversible [120]. F, Si, Fe, and Al as dopants work as inhibitors for the transformation process, and they slow down the process from anatase to rutile [120]. Alghamdi et al. report no sign of overlapping HOMO levels between H_2O_2 and TiO_2 rutile (110) surface; this in addition to the high adsorption energy could explain why water splitting is slow [121].

3.6. Collected Data

In Table 1 we have tabulated the bandgap, photocurrent density, hydrogen, and oxygen production rate from the articles discussed in this section.

Table 1. This table displays the theoretical bandgap values for different doped TiO_2 materials and for a few of these the H_2 production rate is presented if published.

Nanomaterial	Bandgap [eV]	Ref.
Ag doped TiO_2	2.312	[88]
Au doped TiO_2	0.996	[88]
Pt doped TiO_2	0.754	[88]
Pd doped TiO_2	0.363	[88]
Ru doped TiO_2	0.176	[88]
Wet TiO_2 (001)	1.8571	[89]
Pt doped Wet TiO_2 (001)	1.4546	[89]
Ru doped Wet TiO_2 (001)	0.1636	[89]
Co doped Wet TiO_2 (001)	0.0539	[89]
Ru clusters on TiO_2	NA	[90]
Anatase TiO_2	3.05	[91]
Pt adsorbed on TiO_2	3.06	[91]
Pd adsorbed on TiO_2	3.05	[91]
Rh adsorbed on TiO_2	2.80	[91]
Ru adsorbed on TiO_2	3.10	[91]
Anatase TiO_2	2.98	[92]
Rutile TiO_2	2.78	[92]
aTiO_2	NA	[93]
Cu + N co-doped TiO_2	NA	[94]
Cu doped anatase TiO_2 (101)	NA	[95]
Cu doped anatase TiO_2 (101)	NA	[15]
Co-doped $SrTiO_3$	3.07	[96]
N-doped aTiO_2	2.25	[97]

Table 1. *Cont.*

Nanomaterial	Bandgap [eV]	Ref.
S-doped anatase TiO_2	2.33	[98]
Nb-doped anatase TiO_2	2.25	[98]
(S, Nb)-doped anatase TiO_2	2.15	[98]
TiO_2 hollow spheres doped with Mg	NA (H_2 production rate: 850 μmol/h/g. O_2 production rate: 425 μmol/h/g)	[99]
TiO_2 doped by lanthanides	NA	[100]
C@O-doped TiO_2	3.019	[102]
C@gap-doped TiO_2	3.021	[102]
Nd@Ti-doped TiO_2	3.032	[102]
Nd@gap-doped TiO_2	2.353	[102]
C@O&Nd@Ti-doped TiO_2	2.372	[102]
C&Nd@gap-doped TiO_2	2.850	[102]
TiO_{2-X}	2.6 (H_2 production rate: 46.9 μmol/h/g)	[103]
g-CS@TiO_{2-X}	2.5 (H_2 production rate: 255.2 μmol/h/g)	[103]
g-CS+TiO_{2-X}	2.3 (H_2 production rate: 68.3 μmol/h/g)	[103]
Se(IV) ion doped TiO_2	2.85	[104]
N-doped TiO_2	3.06	[105]
Co-doped TiO_2	2.92	[105]
Co-1N-doped TiO_2	2.91	[105]
Co-2N-doped TiO_2	2.90	[105]
Co-3N-doped TiO_2	2.92	[105]
Mesoporous carbonate-doped phase-junction TiO_2 nanotubes	2.69-2.92 (H_2 production rate: 6108 μmol/h/g)	[106]
B-doped TiO_2	2.40	[108]
S-doped TiO_2	2.23	[108]
C-doped TiO_2	2.53	[108]
P-doped TiO_2	2.30	[108]
N-doped TiO_2	2.51	[108]
F-doped TiO_2	2.61	[108]
Cl-doped TiO_2	2.34	[108]
N-TiO_2	2.94	[109]
Cu-TiO_2	3.22	[109]
(Cu, N)-TiO_2	2.96	[109]
TiO_2/g-C_3N_4	2.34	[109]
N-TiO_2/g-C_3N_4	2.31	[109]
Cu-TiO_2/g-C_3N_4	2.23	[109]
(Cu, N)-TiO_2/g-C_3N_4	2.26	[109]
g-C_3N_4/TiO_2	2.21	[110]
(C, N)-doped rutile TiO_2	2.59	[111]
Rh, Nb co-doped TiO_2	NA	[112]

Table 1. *Cont.*

Nanomaterial	Bandgap [eV]	Ref.
S, N, or S+N doped TiO_2 anatase (101) nanotubes	2.78–4.32	[113]
S-doped TiO_2	2.72	[114]
Sc-doped three-layer fluorite structured TiO_2	4.00	[115]
V-doped three-layer fluorite structured TiO_2	3.95	[115]
Cr-doped three-layer fluorite structured TiO_2	3.98	[115]
Mn-doped three-layer fluorite structured TiO_2	3.66	[115]
Fe-doped three-layer fluorite structured TiO_2	3.39	[115]
Co-doped three-layer fluorite structured TiO_2	4.01	[115]
Ni-doped three-layer fluorite structured TiO_2	4.20	[115]
Cu-doped three-layer fluorite structured TiO_2	4.20	[115]
Zn-doped three-layer fluorite structured TiO_2	3.60	[115]
4d metals doped TiO_2 nanotubes	2–4	[116]
Three-layer TiO_2 (101) nanotubes	3.83	[117]
Six-layer TiO_2 (101) nanotubes	4.17	[117]
Nine-layer TiO_2 (001) nanotubes	3.95	[117]
Six-layer TiO_2 (001) nanotubes	4.15	[117]
Facer dependency of TiO_2	NA	[118]
TiO_2	NA	[119]
Phase stability in TiO_2	NA	[120]
Rutile TiO_2	NA	[121]
$aTiO_2$	2.70–2.85	[14]

As Table 1 clearly illustrates, the major focus for theoretical studies had been on bandgap calculations and alterations, but these numerical results had deviations from the results from experimental research. The majority of dopants introduced intermediate bandgaps to the structure, thus reducing the needed phonon energy for excitation. We find that by choosing the correct dopant, the effective bandgap can be lowered to 2.15 eV by co-doping TiO_2 with sulfur and niobium [98]. Other promising candidates are N-doped $aTiO_2$ (2.25 eV) [97] and the more complex g-C_3N_4/TiO_2 (2.21 eV) [110]. A general problem with the computational studies we have reviewed is the lack of a successful descriptor of the hydrogen evolution reaction (HER) activity, however, the hydrogen adsorption free energy, ΔG_H, has shown promises [122].

4. Experimental Research

Recent advances in fabrication techniques have made it possible to deposit ultra-thin films, various-sized nanoparticles, and to create nanowires, nanorods, nanobelts, etc. This has made it possible to utilize interesting properties of nanostructure and improve TiO_2 photocatalysts.

4.1. Metal Dopants

An interesting phenomenon that could be exploited to increase the solar absorption is the surface plasmon resonance (SPR) effect and localized surface plasmon resonance (LSPR) effect, where metal nanoparticles absorb incoming light outside the bandgap of the catalyst. The generated electrons will then be transferred to the surface of the photocatalyst and take part in the oxidation and reduction of the water molecules. To achieve this, one must add metal nanoparticles to the surface of the photocatalyst and let them absorb incoming radiation. Several attempts utilizing metal dopants on TiO_2 photocatalysts have revealed an increase in light absorption due to SPR/LSPR.

Zhao Li et al. worked on aluminum-doped TiO_2, and they report an increased PEC efficiency due to the LSPR effect [123]. Interestingly enough, they also found that an ultrathin (0.8–2.5 nm) layer of Al_2O_3 is formed naturally, which works as a protective layer against Al NPs corrosion and in reducing the surface charge recombination [123].

A similar increase in light absorption due to SPR and LSPR can be found using Co, Ni, titanium nitride (TiN), Au, Cu, or Ag dopants [124–129]. Nickel was also found to improve the separation of electron–hole pairs [125], while TiN assisted with charge generation, separation transportation, and injection efficiency [126]. Another advantage of the Ag nanoparticles is that they lower the charge carrier recombination rate [129]. In their research on Au dopants, Jinse Park et al. used ZnO–TiO_2 nanowires and found that the nanowires themselves excel in charge separation and transportation [127]. Shuai Zhang et al. used a Cu doped TiO_2 nanowire film, which showcased clear improvement in photocurrent density due to the unique architecture [128].

In a similar experiment, Jie Liu et al. used Co_3O_4 quantum dots on TiO_2 nanobelts and achieved H_2 and O_2 production rates of 41.8 and 22.0 µmol/hg [130]. The QDs favored transfer and accommodation of photo-generated electrons, in addition, to inhibit the recombination of charge carriers [130].

Doping could also induce a Schottky junction in the photocatalyst, which could help increase the charge transfer and help separate the photogenerated electrons and holes. He et al. showed this, using TiO_2 nanowire decorated with Pd NPs and achieving a photocurrent density of 1.4 mA/cm^2 [131]. The use of platinum within TiO_2 based photocatalysts is well known, and Lichao Wang et al. showed that by creating a Pt/TiO_2 photocatalyst, an H_2 production rate of 7410 µmol/gh is achievable [132].

Complex dopants have also been used on TiO_2, in addition to nanostructures. This makes it possible to combine the properties of the various dopants on TiO_2. In an attempt to increase the hydrogen production of TiO_2, Ejaz Hussain et al. doped TiO_2 with Pd–BaO NPs [133]. They achieved an H_2 production of 29.6 mmol/hg in a solution of 5% ethanol and 95% water [133]. Hussain et al. took advantage of the inherent high catalytic activity of the Pd nanoparticles, and the fact that barium oxide (BaO) enhances the electron transfer from the semiconductor band to the Pd centers [133]. In a similar approach, cadmium sulfide (CdS) was incorporated into a TiO_2 photoanode [134]. This utilized the suppression of electron-hole recombination and efficient charge separation/diffusion due to the nanorod structure, in addition to the SPR effect from the dopants [134]. Instead of doping TiO_2 only with CdS, it could be combined with tin (IV) oxide (SnO_2) nanosheets. The reason for this is that TiO_2 reduces the charge recombination between Cds and SnO_2 [135]. Thus, the number of electrons and holes reaching the surface and participating in the reduction or oxidation process increases.

It is also possible to dope TiO_2 with Ti^{3+} and Ni to improve the overall efficiency; in fact, Ti^{3+}/Ni co-doped TiO_2 nanotubes have a bandgap of 2.84 eV [136]. This is roughly 12% narrower than that of pure TiO_2 and could be explained by the SPR effect.

Lately, there has been some research devoted to black titanium dioxide. Mengqiao Hu et al. used Ti^{3+} self-doped mesoporous black TiO_2/SiO_2/g–C_3N_4 sheets [137]. The system has a bandgap of ~2.25 eV and photocatalytic hydrogen evolution of 572.6 μmol/gh. This is all due to the unique mesoporous framework enhancing the adsorption of pollutants and favoring the mass transfer, Ti^{3+} self-doping reducing the bandgap, and extending the photoresponse to the visible light region [137].

Through modifying the TiO_2 NPs with 2D molybdenum disulfide ($MoSe_2$), Lulu Wu et al. achieved a hydrogen production rate of 5.13 μmol/h for samples with 0.1 wt.% MoSe2 [138]. They created $MoSe_2$ nanosheets, which were then combined with TiO_2 nanoparticles to create an efficient photocatalyst (Figure 8), by taking advantage of the wide light response and rapid charge migration ability of 2D nanosheets $MoSe_2$. A slightly different approach would be to wrap rutile TiO_2 nanorods with amorphous $Ta_2O_xN_y$ to achieve an optical bandgap of 2.86 eV with band edge positions suitable for water splitting [139].
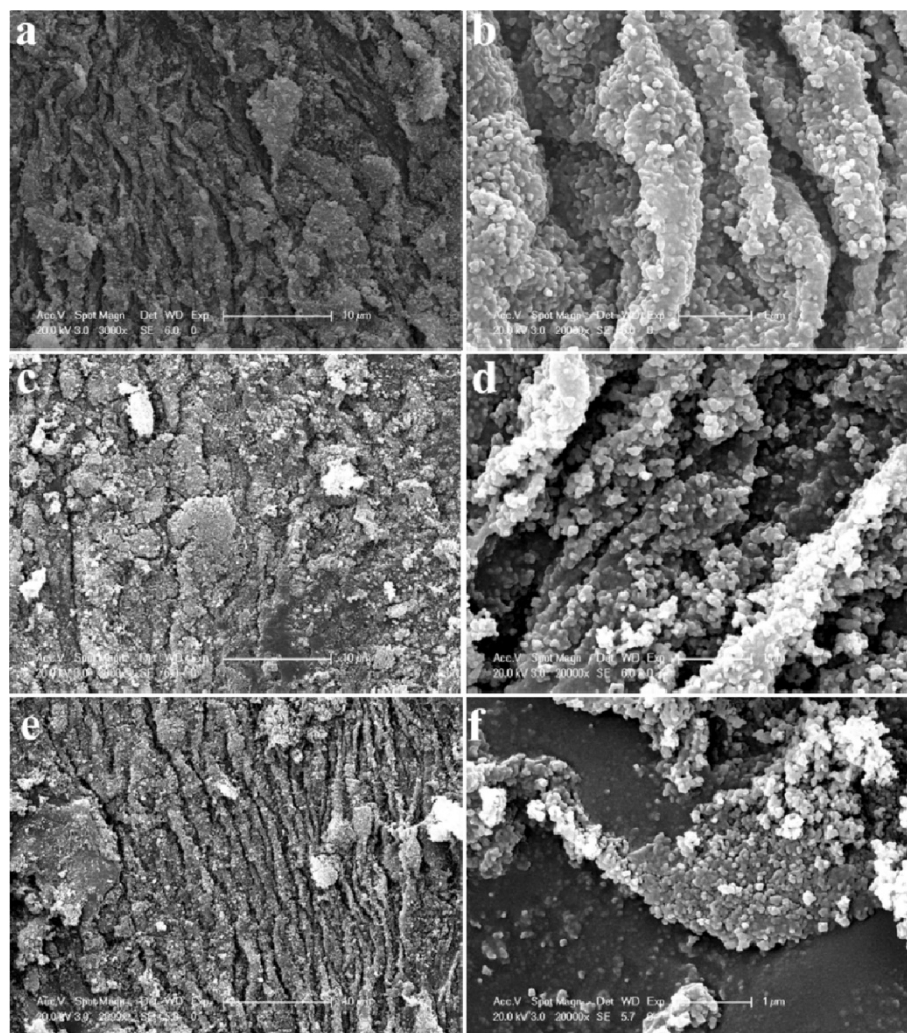

Figure 8. SEM images of $MoSe_2$ with TiO_2 nanoparticles synthesised using a simple hydrothermal method; (**a,b**) 0.025%, (**c,d**) 0,05%, and (**e,f**) 0.1% mass ratio of $MoSe_2$:TiO_2. Reprinted with permission from [138]. Copyright 2019, with permission from Elsevier.

Bismuth vanadate ($BiVO_4$), iron (III) oxide/hematite (Fe_2O_3), and bismuth ferrite ($BiFeO_3$) are materials with interesting properties for solar-driven water splitting. They all have low bandgaps, which could help with visible light absorption, and are both simple and inexpensive materials [140–142]

Xin Wu et al. utilized $BiFeO_3$ (BFO) on top of TiO_2 and found a photocurrent density as high as 11.25 mA/cm^2, 20 times higher than that of bare TiO_2 [143]. The improvement is mainly due to the heterostructure of BFO/TiO_2 and the ferroelectric polarization due to the introduction of BFO, which could lead to upward bending at the interface and thus effectively drive the separation and transportation of photogenerated carriers [143].

Bismuth vanadate is most often used together with a dopant. For example, Jia et al. used W to dope TiO_2/$BiVO_4$ nanorods and obtained a bandgap of 2.4 eV [144]. In addition, Wengfeng Zhou et al. synthesized an ultrathin Ti/TiO_2/$BiVO_4$ nanosheet heterojunction [145]. It had an enhanced photocatalytic effect due to the formation of a built-in electric field in the heterojunction between TiO_2 and $BiVO_4$ [145]. Using Co, Pi Quan Liu et al. modified a TiO_2/$BiVO_4$ composite photoanode, which shows improved visible light absorption and a more efficient charge transfer relay [146]. By combining FeOOH/TiO_2/$BiVO_4$, Xiang Yin et al. created a photoanode that led to a hydrogen production rate of 2.36 μmol/cm^2 after testing for 2.5 h [147].

However, it is possible to use $BiVO_4$ without a dopant BiV because O_4 and TiO_2 naturally complement each other. It allows for the exploitation of the excellent absorption properties of $BiVO_4$ to produce highly reductive electrons through TiO_2 sensitization under visible light [148]. Another example of this is how Ahmad Radzi et al. deposited $BiVO_4$ on TiO_2 to increase PEC efficiency [149].

Hematite is usually combined with more complex structures, for example, 3d ordered urchin-like TiO_2@Fe_2O_3 arrays [150]. Using these arrays Chai et al. reported a photocurrent density of 1.58 mA/cm^2 at 1.23 V vs. reversible hydrogen electrode (RHE) [150]. This is a clear improvement compared to pristine TiO_2.

A different approach is to use amorphous Fe_2O_3 with TiO_2 and silicon (Si). With this method, Zhang et al. achieved a photocurrent density of 3.5 mA/cm^2 at 1.23 V vs. RHE [151]. It is also possible to use TiO_2 as the dopant on hematite. Fan Feng et al. decorated a hematite PEC with TiO_2 at the grain boundaries [152] that increased the charge carrier density and improved the charge separation efficiency, resulting in a photocurrent density of 2.90 mA/cm^2 at 1.23 V vs. RHE [152].

However, one could also use a simple TiO_2/Fe_2O_3 heterojunction, which Deng et al. found improved the photocurrent density due to improved separation and transfer of photogenerated carriers [153].

A few studies are also reported on on metal-organic frameworks (MOFs) in cooperation with TiO_2.

Yoon et al. coated TiO_2 nanorods (NRs) with NH_2–MIL-125(Ti) and achieved a photocurrent density of 1.62 mA/cm^2 [154]. The high photocurrent can be explained by several factors: the large surface area and crystallinity of TiO_2 NRs, which leads to effective light absorption and charge transport. Or the moderate bandgap of MIL(125)–NH_2, the uniform and conformal coating of the MIL layer, and the efficient charge carrier separation and transportation through the type (II) band alignment of TiO_2 and MIL(125)–NH_2.

4.2. Non-Metal Dopants

Metal dopants could act as recombination centers for electrons and holes and thus lowering the overall efficiency of the photocatalyst [155]. Thus, a large number of research studies have been going on toward doping TiO_2 with non-metal dopants, for example, Si, S, C, F, and N.

Yang Lu et al. doped TiO_2 nanowires with earth-abundant Si and achieved an 18.2 times increase in the charge carrier density, which was better than in N and Ti (III) doped TiO_2 [156]. The increase in visible light photocatalytic activity is due to the enhanced electron transport, because of higher charge-carrier density, longer electron lifetime, and

larger diffusion coefficient in Si-doped TiO_2 NWs [156]. High-quality graphene could be of use in water splitting as quantum dots on rutile TiO_2 nanoflowers because they are highly luminescent and can absorb UV and visible light up to wavelengths of 700 nm [157]. Bellamkonda et al. found that multiwalled carbon nanotubes–graphene–TiO_2 (CNT–GR–TiO_2) could achieve a hydrogen production rate of 29 mmol/hg (19 mmol/hg for anatase TiO_2) [158]. They also had an estimated solar energy conversion efficiency of 14.6% and a bandgap of 2.79 eV, which was due to the generation of Ti^{3+} and oxygen vacancies within the composite [158]. TiO_2 absorbs UV light due to its inherent large bandgap, Qiongzhi Gao et al. [159] utilized this and doped TiO_2 with hydrogenated F. The hydrogen-treated F atoms increased both UV and visible light absorption. When TiO_2 is doped with sulfur, an abundant element, a bandgap of 2.15 eV can be expected [160]. N and lanthanum (La) co-doping of TiO_2 does not reduce the bandgap, but the photocatalytic effect is seen to be enhanced due to an increase in surface nitrogen and oxygen vacancies [161].

4.3. Improved Production Methods

As discussed, although there are several options in order to dope TiO_2 with metals and non-metals, the research community has devoted much energy to improving the characteristics of TiO_2 photocatalysts through appropriate synthesis conditions. It is possible to achieve improved mechanical strength, enhanced composite stability, surface area, roughness, and fill factor for TiO_2 by using branched multiphase TiO_2 [162].

Treating TiO_2 with Ar/NH_3 during the fabrication process, which could improve the density of the charge carrier and broaden the photon absorption both in the UV and visible light regions [163]. An increase in density of states at the surface and a 2.5-fold increase in photocurrent density at 1.23 vs. RHE could be achieved by anodizing and annealing TiO_2 during the fabrication process [164]. Ning Wei et al. showed that by controlling TiO_2 core shells, it was possible to achieve a bandgap of 2.81 eV, and had an H_2 evolution rate of 49.2 μmol/(h cm) [165].

Huali Huang et al. looked into the effect of annealing the atmosphere on the performance of TiO_2 NR [46]. Oxygen, air, nitrogen, and argon were used as the different atmospheres. The same rutile phase was observed, but it resulted in different H_2 activities. Samples annealed in argon showed the highest photocurrent density of 0.978 mA/cm^2 at 1.23 V vs. RHE [46], an increase of 124.8% compared to the oxygen annealed samples. It was found that the density of oxygen vacancies in the samples increased with the decrease in oxygen in the annealing atmosphere [46]. The increase in oxygen vacancies enhances visible light absorption and increases the electron conductivity (inhibits recombination of the charge carriers) [46].

Aleksander et al. examined what would happen if the substrate, which TiO_2 was fabricated on was changed [166]. The authors lowered the optical reflection by using black silicon, which in turn increased the light collection [166]. They also found that the addition of noble metals could induce SPR in the visible light region [166].

By combining improved production methods and doping/co-doping with metals/non-metals, TiO_2 could be realized as an efficient photocatalyst. Fu et. al. showed that by controlling the HCl concentration during the synthesis process, it was possible to synthesize well-crystallized rutile TiO_2 nanorods with special aspect ratios [167]. They proposed a process, as shown in Figure 9, for synthesizing rutile TiO_2 with different aspect ratios. Rutile TiO_2 nanorods with small aspect ratios were formed by placing titanium tetrachloride ($TiCl_4$) in liquid hydrochloric acid (HCl) before undertaking hydrothermal treatment. The key factors were the presence of Cl^- and H^+ at high temperature and pressure. For the synthesis of nanorods with medium/large aspect ratios titanium butoxide (TBOT) was added dropwise to HCL (aq.)/NaCl (aq.) This created rutile/anatase crystal seeds, which were placed in HCl (aq.) for the final growth process. They concluded that with decreasing aspect ratios, the photocatalytic water splitting activity would increase for TiO_2 nanorods [167].
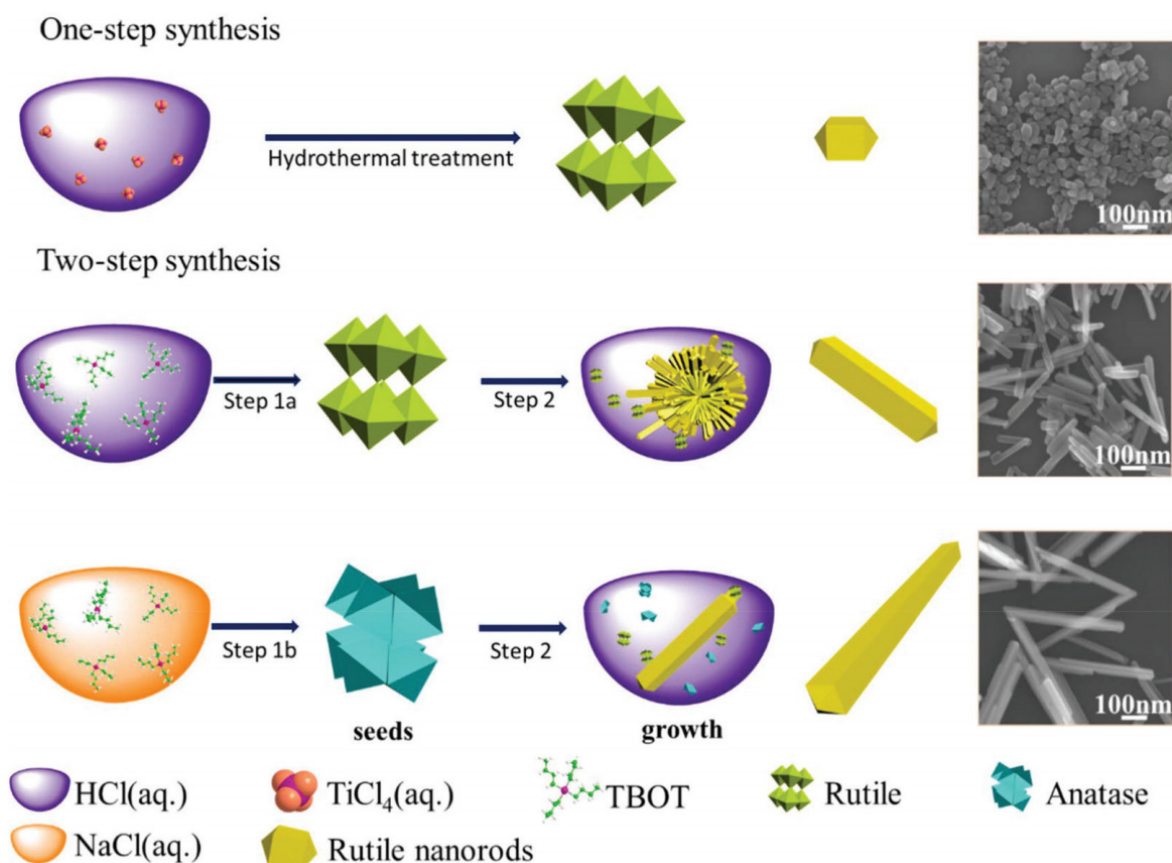
Figure 9. Schematic illustration of the synthesis of rutile TiO$_2$ with specific (small, medium, and large) aspect ratios. Reprinted with permission from [167]. Copyright 2018, with permission from RSC.

4.4. Collected Data

We present in Table 2 the obtained bandgap, photocurrent density, H$_2$, and O$_2$ production rate values from experimental studies that are reviewed here.

We see from the data presented in Table 2 that it is possible to adjust the properties of TiO$_2$ photocatalysts by doping or through structural changes. For example, Elbakkay et al. achieved a bandgap of 2.15 eV using an S–TiO$_2$/S-reduced graphene oxide catalyst [160]. Both theoretical and experimental studies point at sulfur as a possible dopant for TiO$_2$ that could drastically reduce the effective bandgap of the photocatalyst. In general, theoretical studies tend to focus on simpler structures and doping of TiO$_2$, while experimental research has moved on toward more complex structures of TiO$_2$ that consist of several layers, materials, and nanostructures.

It is clear from Table 2 that the various solutions and potentials are used for measuring HER, and presenting photocurrent density in different ways is an issue that makes the direct comparison difficult. This hampers the evaluation of the most promising TiO$_2$ structure for photocatalytic activity. Likewise, the theoretical studies use different models and approximations that make it difficult to compare the numerical results for different TiO$_2$ structures. Combined theoretical and experimental study along with the establishment of standards, for example, for measuring H$_2$ production, would help the path to develop TiO$_2$ photocatalysts towards commercial realization.

Table 2. This table displays the bandgap, photocurrent density, and H$_2$ production rate experimentally achieved for doped/modified TiO$_2$ structures in articles reviewed in this study.

Nanomaterial	Bandgap [eV]	Photocurrent Density at 1.23 V vs. RHE [mA/cm^2]	H$_2$ Production Rate 1.5G Sunlight Bias at 1.23 vs. RHE	O$_2$ Production Rate 1.5G Sunlight Bias at 1.23 vs. RHE	Ref.
TiO$_2$@Fe$_2$O$_3$/TiO$_2$	2.2	1.58, and 3.6 at 1.6 V vs. RHE	NA	NA	[150]
α-Ta$_2$O$_x$N$_y$ enwrapped TiO$_2$ rutile nanorods	2.86	1.32	244.2 mmol/m^{2}h	112.7 mmol/m^{2}h	[139]
Ag-TiO$_2$-NR05	2.64	0.08 and 0.10 mA/cm^2 at 1.2 and 1.6 V vs. RHE	NA	NA	[129]
W-TiO$_2$/BiVO$_4$ nanorods	2.4	2.5	41 µmol/h	NA	[144]
Branched multiphase TiO$_2$	3.04	0.95	NA	NA	[162]
Co$_3$O$_4$ quantum dots on TiO$_2$	3.07	0.0005	41.8 µmol/h/g	22.0 µmol/h/g	[130]
Co-Pi modified 3D TiO$_2$/BiVO$_4$	NA	4.96 at 0.63 V vs. Ag/AgCl	NA	NA	[146]
Co doped TiO$_2$ nanotubes	2.88	1.0	NA	NA	[124]
Controllable TiO$_2$ core shells	2.81	3.88	49.2 µmol/cm^{2}h	25.2 µmol/cm^{2}h	[165]
A-Fe$_2$O$_3$/TiO$_2$/Si	NA	3.5	NA	NA	[151]
Al@TiO$_2$	NA	NA	NA	NA	[123]
Si-doped TiO$_2$ nanowires	NA	NA	NA	NA	[156]
Three-layer (SiO$_2$, Al$_2$O$_3$, and TiO$_2$) structure with Au particles for LSPR	NA	NA	NA	NA	[168]
BiFeO$_3$/TiO$_2$	NA	11.25	NA	NA	[143]
Graphene QDs decorated rutile TiO$_2$ nanoflowers	NA	~0.32 at 0.5 V vs. Ag/AgCl	NA	NA	[157]
Hierarchical TiO$_2$/Fe$_2$O$_3$	NA	1.79	NA	NA	[153]
CNT-GR-TiO$_2$	2.79	NA	29 mmol/h/g	NA	[158]
SnO$_2$ nanosheets with TiO$_2$ and CdS QD	NA	4.7 at 0V vs. Ag/AgCl	NA	NA	[135]
TiO$_2$ nanotubes treated with Ar/NH$_{3+}$	NA	1 at 1.18 V vs. RHE	NA	NA	[163]
TiO$_2$ nanowire decorated with Pd	NA	1.4	NA	NA	[131]
NH$_2$-MIL-125(Yi) on TiO$_2$ nanorods	NA	1.62	NA	NA	[154]
Ni-doped TiO$_2$ nanotubes	NA	0.93 at 0 V vs. Ag/AgCl	NA	NA	[125]
N doped La/TiO$_2$	2.96–2.99	NA	8.25 µmol/h/g	NA	[161]

Table 2. *Cont.*

Nanomaterial	Bandgap [eV]	Photocurrent Density at 1.23 V vs. RHE [mA/cm^2]	H$_2$ Production Rate 1.5G Sunlight Bias at 1.23 vs. RHE	O$_2$ Production Rate 1.5G Sunlight Bias at 1.23 vs. RHE	Ref.
TiN boosted N doped TiO$_2$	NA	3.12	NA	NA	[126]
CuO@TiO$_2$ nanowires	NA	0.56	NA	NA	[128]
Pd-BaO NPs on TiO$_2$	NA	NA	29.6 mmol/h/g	NA	[133]
S-TiO$_2$/S-RGO	2.15	3.36 at 1 V vs. Ag/AgCl	NA	NA	[160]
Anodized and H$_2$ annealed TiO$_2$	NA	2.5 fold TiO$_2$	NA	NA	[164]
TiO$_2$ NPs modified with 2D MoSe$_2$	NA	NA	5.12 μmol/h	NA	[138]
Ultrathin Ti/TiO$_2$/BiVO$_4$	NA	5.8 μa/cm^2 at 0.5 V vs. Ag/AgCl	NA	NA	[145]
TiO$_2$ on black Si	NA	NA	NA	NA	[166]
ZnO-TiO$_2$ core-shell nanowires decorated with Au NPs	NA	1.63	NA	NA	[127]
TiO$_2$/CdS system	2.25	30 mA/cm^2 (at 1 V vs. Ag/AgCl) under 1.5 AM	1.3 mmol/cm^{2}h	NA	[134]
FeOOH/TiO$_2$/BiVO$_4$	NA	3.21	2.36 μmol/cm^2	1.09 μmol/cm^{2}h	[147]
hematite PEC decorated with TiO$_2$ at the grain boundaries	NA	2.90	NA	NA	[152]
the effect of annealing atmosphere on the performance of TiO$_2$ NR	NA	0.978	NA	NA	[46]
Ti^{3+}/Ni co-doped TiO$_2$ nanotubes	2.84	0.87	NA	NA	[136]
Hydrogenated F-doped TiO$_2$	3.0	NA	3.76 mmol/h/g	NA	[159]
BiVO$_4$ deposited on TiO$_2$	NA	35 μ under 100 mW/cm^2 in 0.5M Na$_2$SO$_4$	NA	NA	[149]
BiVO$_4$ used together with TiO$_2$	NA	~0.3 at 1.0 V vs. RHE	NA	NA	[148]
Pt/TiO$_2$(anatase) photocatalyst	NA	NA	7410 μmol/h/g	5096 μmol/h/g	[132]
Ti^{3+} self-doped mesoporous black TiO$_2$/SiO$_2$/g-C$_3$N$_4$ sheets	~2.25	NA	NA	NA	[137]
Rutile TiO$_2$ nanorods with small aspect ratio	NA	NA	1229 μmol/h/g	549 μmol/h/g	[167]
Rutile TiO$_2$ nanorods with medium aspect ratio	NA	NA	783 μmol/h/g	369 μmol/h/g	[167]
Rutile TiO$_2$ nanorods with large aspect ratio	NA	NA	549 μmol/h/g	252 μmol/h/g	[167]

As we can observe from the results presented so far, great steps have been taken to make TiO_2 photocatalysts for water splitting a viable technology for green hydrogen production. However, even though the progress has been rapid over the past decade there are still obstacles in the way to large-scale production facilities.

Coordinated theoretical and experimental study of TiO_2 structures for enhancing the electronic, optical, and physical properties will help achieve the goal of efficient low-cost photocatalysts for water splitting.

In general, during the synthesis of the photocatalysts, there is uncertainty in the exact composition and structure of the compound [169,170]. This is especially prevalent for doping and the location of the dopants in the compound. For example, if the dopants are too deep or too shallow (on the surface), they will behave as recombination centers and thus reduce the overall solar to hydrogen efficiency [171]. The selection of deposition techniques for TiO_2 structures will have an effect on the performance as these techniques have advantages and disadvantages. For example, chemical vapor deposition (CVD) and physical vapor deposition (PVD) produce homogenous and flexible microstructure and super hard materials, but the drawbacks are challenges with deposition rate, maintenance cost, and the size of the component. Thermal spraying has the advantage of fast deposition rates, large components, and ease of exploitation, but does not produce coatings of the same quality as CVD, electrodeposition, or PVD [172]. In other words, there is always the dilemma of choosing the correct deposition method and figuring out how it could affect the performance of the material. The research community employs a variety of techniques to characterize the material, infrared spectroscopy, Raman spectroscopy, scanning electron microscopy (SEM), X-ray spectroscopy, etc. Because the reviewed studies employ different characterization methods to verify, for example, the bandgap of TiO_2 structures, a comparison of results in different studies becomes challenging. Another challenge is that experiments are not carried out under standardized conditions (e.g., with constant irradiance and homogeneous light distribution), the assessment of the real progress achieved with modified TiO_2 is often difficult. Furthermore, comparisons between pristine TiO_2 and enhanced photocatalysts are frequently biased because samples selected as reference materials present a relatively low photoactivity [173].

Computational modeling and simulations can help relieve some of these issues, although it comes with its own limitations. One advantage of theoretical simulations is that it is possible to create the exact structure you want to work on. Thus, we can investigate specific attributes and properties by fine-tuning the structure and composition of the compound. Moreover, the calculation of the H_2 and O_2 production is not based on measurement conditions, which makes results easier to compare.

4.5. Production Facilities

The aforementioned challenges are not the only ones that the research community faces in using TiO_2 as the photocatalytic material for water splitting. Unfortunately, there is still a lack of scalable systems that could produce hydrogen in an economically feasible manner, even with an efficient catalyst [174]. Pinaud et. al. proposed and discussed the economic feasibility of four different designs of photocatalytic water splitting plants and the schematics are shown in Figure 10 [175].

Type 1 is a single bed particle suspension reactor and it is the simplest of the four. It consists of a low-lying horizontal plastic bag containing a slurry of photoactive particles in an electrolyte. The plastic bag is designed to allow light to penetrate, while it retains the electrolyte, photoactive particles, and evolved gases.

The Type 2 reactor is a dual bed with particle suspension, and it is similar to that of the Type 1 reactor. However, the biggest difference is that separate beds are used for H_2 and O_2 production.
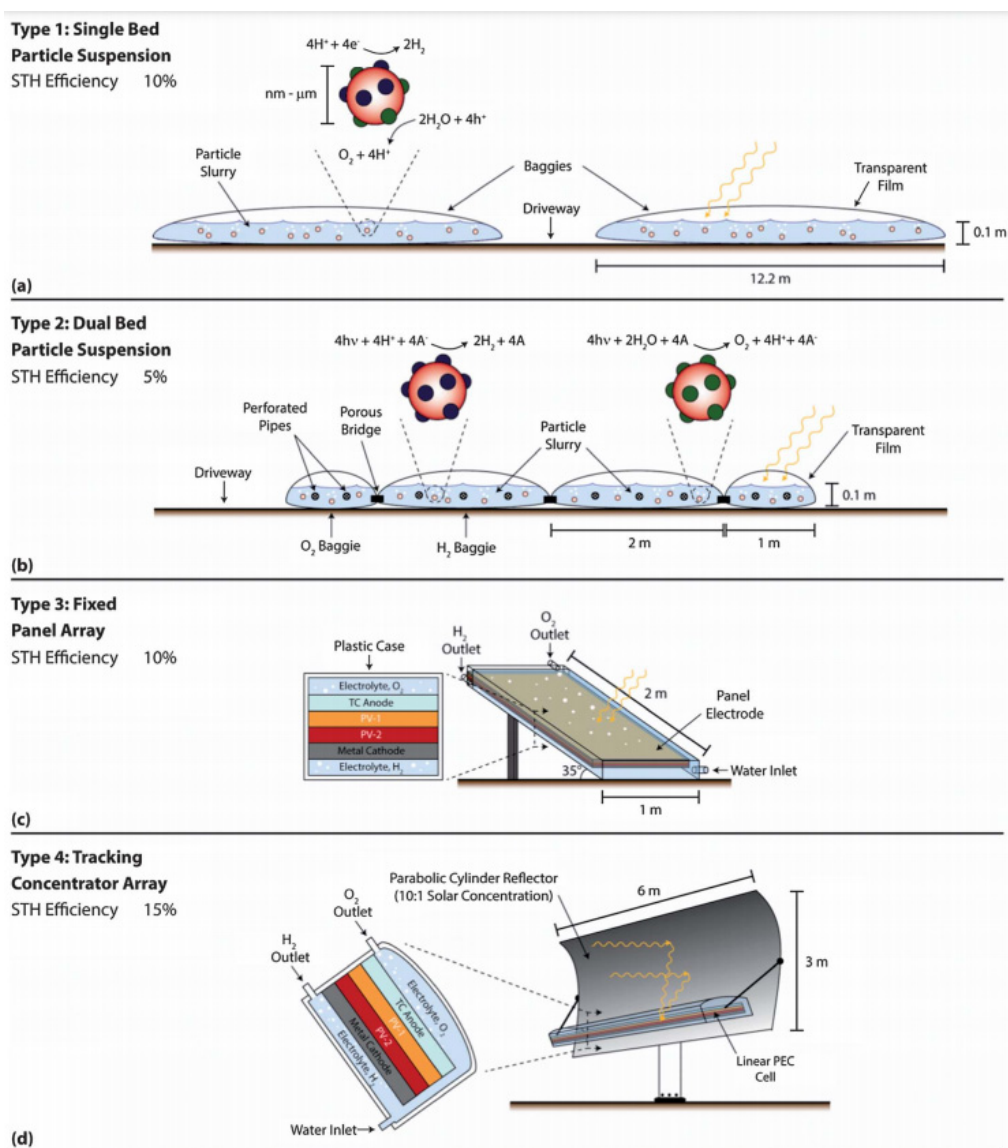
Figure 10. Schematic of the four different reactors. (**a**) Cross section of the Type 1 reactor showing the particle slurry contained by the baggies and separated by the driveway, (**b**) Type 2 reactor cross section with separate oxygen and hydrogen baggies connected by a porous bridge, (**c**) Type 3 reactor utilizing a photoelectrochemical (PEC) cell instead of photocatalytic water splitting (PWS) being directed toward the sun and (**d**) Type 4 reactor design that combines the PEC cell with an offset parabolic solar concentrator. Drawing not to scale. Reused with permission from [175]. Copyright 2013, with permission from Royal Society of Chemistry.

The third option, named Type 3 reactor, is a fixed panel array, which consists of an integral planar electrode with multiple photoactive layers sandwiched between two electrodes. The entire system is within a transparent plastic electrolyte reservoir. The final alternative is the Type 4 reactor, which is a tracking concentrator array that uses an offset parabolic cylinder array to focus sunlight on a linear PEC cell receiver and has two-axis steering to track the daily movement of the sun [175].

In general, it was found that the key component for realizing these designs was to improve the solar to hydrogen efficiencies [175]. However, there are also other limitations, such as safety issues with the H_2 and O_2 gas mixture, how to split and collect the H_2 and O_2 gasses, a lack of general understanding of how the photocatalyst particle works, the mechanical integrity of the plastic bags, etc. [175].

5. Conclusions and Long-Term Outlook

Even though considerable progress has been made in the development of solar-driven water splitting with TiO_2 as the photocatalyst, we believe there are four major challenges the research community must tackle before it becomes a viable technology.

The first challenge is the lack of a standard way to express the hydrogen production rates with varying photocatalytic materials. Research groups have been presenting these generations' rates in different ways that make the comparison challenging. As seen in the literature presented here, the measured hydrogen evolution rates depend on specific details of the experimental setup, such as the spectrum of the light source, the light intensity at the sample, co-catalyst selection, size of the potential, and type and selection of the solution. Suggestions and solutions for standard experimental setups are also needed. However, reporting the apparent quantum yield (AQY) instead of only the gas evolution could be a part of the solution [176,177]. This will help bridge the gap between experimental and theoretical results. Computational modeling has some of the same challenges as the model, assumptions, approximations, and software used will affect the numerical results that make the comparison of results demanding. The missing piece here is calculations of the hydrogen and oxygen evolution rates, and an alternative can be studying the Volmer reaction, the Tafel reaction or the Herovsky reaction, and the Gibbs free energy [178,179].

The second challenge is the material TiO_2 and its wide bandgap of 3.2 eV, which is in the ultraviolet section of the visible light spectrum. This means that 97% of the energy coming from the sun is not usable for TiO_2 photocatalysts. There have been several attempts to lower the bandgap of TiO_2, both experimentally and theoretically, which have been successful. However, the most successful experimental works are based on complex nanostructures or layered structures that are difficult and expensive to create at a larger scale. Computational modeling has in general focused more on various dopants and doping percentages. Unfortunately, the best results are seen when using noble metals or expensive metals. However, sulfur doping could be a solution to this problem. Combined TiO_2 with other earth-abundant materials as MoS_2 or WS_2 could be better photocatalysts in the future [180,181].

The third challenge is the lack of research combining experimental research with theoretical simulations to optimize the characteristics of TiO_2 structures for photocatalytic applications. This is a weakness in the current research as theoretical modeling and simulation could work as a great screening tool for the experimentalists, reducing their workload. Theoretical research could also help with the fundamental understanding of the process involved in solar-driven water splitting. By combining the two methods, it is easier to see the inner workings of the photocatalyst and to determine where improvement is needed. Moreover, computational work requires experimental verification and for validating the numerical results.

The final challenge is the lack of scalable systems that could produce hydrogen in an economically feasible manner, even with an efficient catalyst [174]. There is currently a lack of scalable and functional production facilities. The ones that do exist have a solar-to-hydrogen efficiency of 1.8% [182], indicating that further research is needed before photocatalytic water splitting is competitive with other hydrogen production methods. The main factor for the low efficiencies reported for photocatalytic hydrogen production is the low solar-to-hydrogen rates of the photocatalyst itself. An interesting idea is to look into combining TiO_2 with perovskites due to the latter's excellent optoelectronic properties. Naturally, water-insoluble perovskites combined with TiO_2 could be the missing link that solar-driven water splitting needs.

Author Contributions: Conceptualization, H.E. and D.V.; methodology, H.E.; writing—original draft preparation, H.E.; writing—review and editing, H.E., S.B., P.V., S.Y. and D.V.; supervision, D.V. All authors have read and agreed to the published version of the manuscript.

Institutional Review Board Statement: Not Applicable.

References

1. OECD/IEA. World Energy Outlook. 2016. Available online: http://www.iea.org/t&c (accessed on 14 May 2018).
2. Dincer, I.; Zamfirescu, C. *Sustainable Energy Systems and Applications*, 1st ed.; Springer: Berlin/Heidelberg, Germany, 2012; p. XVII. [CrossRef]
3. Tong, Y.; Liang, J.; Liu, H.K.; Dou, S.X. Energy storage in Oceania. *Energy Storage Mater.* **2019**, *20*, 176–187. [CrossRef]
4. Jafari, T.; Moharreri, E.; Amin, A.S.; Miao, R.; Song, W.; Suib, S.L. Photocatalytic water splitting-the untamed dream: A Review of recent advances. *Molecules* **2016**, *21*, 900. [CrossRef]
5. Sharma, P.; Kolhe, M.L. Review of sustainable solar hydrogen production using photon fuel on artificial leaf. *Int. J. Hydrog. Energy* **2017**, *42*, 22704–22712. [CrossRef]
6. Pulido Melián, E.; González Díaz, O.; Ortega Méndez, A.; López, C.R.; Nereida Suárez, M.; Doña Rodríguez, J.M.; Navío, J.A.; Fernández Hevia, D.; Pérez Peña, J. Efficient and affordable hydrogen production by water photo-splitting using TiO_2-based photocatalysts. *Int. J. Hydrog. Energy* **2013**, *38*, 2144–2155. [CrossRef]
7. Bicer, Y.; Dincer, I. Clean fuel options with hydrogen for sea transportation: A life cycle approach. *Int. J. Hydrog. Energy* **2018**, *43*, 1179–1193. [CrossRef]
8. van Biert, L.; Godjevac, M.; Visser, K.; Aravind, P.V. A review of fuel cell systems for maritime applications. *J. Power Sources* **2016**, *327*, 345–364. [CrossRef]
9. International Maritime Organization. Third IMO Greenhouse Gas Study 2014. Available online: http://www.imo.org/en/OurWork/Environment/PollutionPrevention/AirPollution/Pages/Greenhouse-Gas-Studies-2014.aspx (accessed on 14 May 2018).
10. Fujishima, A.; Honda, K. Electrochemical photolysis of water at a semiconductor electrode. *Nature* **1972**, *238*, 37. [CrossRef] [PubMed]
11. Wang, B.; Shen, S.; Mao, S.S. Black TiO_2 for solar hydrogen conversion. *J. Mater.* **2017**, *3*, 96–111. [CrossRef]
12. Chen, X.; Mao, S.S. Titanium dioxide nanomaterials: Synthesis, properties, modifications, and applications. *Chem. Rev.* **2007**, *107*, 2891–2959. [CrossRef]
13. Haggerty, J.E.S.; Schelhas, L.T.; Kitchaev, D.A.; Mangum, J.S.; Garten, L.M.; Sun, W.; Stone, K.H.; Perkins, J.D.; Toney, M.F.; Ceder, G.; et al. High-fraction brookite films from amorphous precursors. *Sci. Rep.-Uk* **2017**, *7*, 15232. [CrossRef] [PubMed]
14. Kaur, K.; Singh, C.V. Amorphous TiO_2 as a photocatalyst for hydrogen production: A DFT study of structural and electronic properties. *Energy Proc.* **2012**, *29*, 291–299. [CrossRef]
15. Zhang, W.; Yin, J.-R.; Tang, X.-Q.; Zhang, P.; Ding, Y.-H. Density functional theory studies on the structural and physical properties of Cu-doped anatase TiO_2 (101) surface. *Phys. E* **2017**, *85*, 259–263. [CrossRef]
16. Morgade, C.I.N.; Cabeza, G.F. First-principles study of codoping TiO_2 systems capable of improving the specific surface area and the dissociation of H_2O to generate H_2 and O_2. *Comput. Mater. Sci.* **2017**, *127*, 204–210. [CrossRef]
17. Press, R.J.; Santhanam, K.S.V.; Miri, M.J.; Bailey, A.V.; Takacs, G.A. Introduction to hydrogen technology. *ChemSusChem* **2009**, *3*, 432.
18. Hoang, D.L.; Chan, S.H.; Ding, O.L. Kinetic and modelling study of methane steam reforming over sulfide nickel catalyst on a gamma alumina support. *Chem. Eng. J.* **2005**, *112*, 1–11. [CrossRef]
19. Ozcan, H.; Dincer, I. Thermodynamic analysis of a combined chemical looping-based trigeneration system. *Energy Convers. Manag.* **2014**, *85*, 477–487. [CrossRef]
20. Steinfeld, A. Solar hydrogen production via a two-step water-splitting thermochemical cycle based on Zn/ZnO redox reactions. *Int. J. Hydrog. Energy* **2002**, *27*, 611–619. [CrossRef]
21. Akkerman, I.; Janssen, M.; Rocha, J.; Wijffels, R.H. Photobiological hydrogen production: Photochemical efficiency and bioreactor design. *Int. J. Hydrog. Energy* **2002**, *27*, 1195–1208. [CrossRef]
22. Liao, C.-H.; Huang, C.-W.; Wu, J.C.S. Hydrogen production from semiconductor-based photocatalysis via water splitting. *Catalysts* **2012**, *2*, 490. [CrossRef]
23. Kudo, A. Photocatalysis and solar hydrogen production. *Pure Appl. Chem.* **2007**, *79*, 1917. [CrossRef]
24. Jang, J.S.; Kim, H.G.; Lee, J.S. Heterojunction semiconductors: A strategy to develop efficient photocatalytic materials for visible light water splitting. *Catal. Today* **2012**, *185*, 270–277. [CrossRef]
25. Moriya, Y.; Takata, T.; Domen, K. Recent progress in the development of (oxy)nitride photocatalysts for water splitting under visible-light irradiation. *Coordin. Chem. Rev.* **2013**, *257*, 1957–1969. [CrossRef]

26. Takata, T.; Jiang, J.; Sakata, Y.; Nakabayashi, M.; Shibata, N.; Nandal, V.; Seki, K.; Hisatomi, T.; Domen, K. Photocatalytic water splitting with a quantum efficiency of almost unity. *Nature* **2020**, *581*, 411–414. [CrossRef]

27. Cho, S.; Jang, J.-W.; Lee, K.-H.; Lee, J.S. Research Update: Strategies for efficient photoelectrochemical water splitting using metal oxide photoanodes. *APL Mater.* **2014**, *2*. [CrossRef]

28. Naik, V.M.; Haddad, D.; Naik, R.; Benci, J.; Auner, G.W. Optical properties of anatase, rutile and amorphous phases of TiO$_2$ thin films grown at room temperature by RF magnetron sputtering. *Mrs Proc.* **2002**, *755*, DD11.12. [CrossRef]

29. Liu, H.; Hsu, Y.; Su, H.; Huang, R.; Hou, F.; Tu, G.; Liu, W. A Comparative study of amorphous, anatase, rutile, and mixed phase TiO$_2$ films by mist chemical vapor deposition and ultraviolet photodetectors applications. *IEEE Sens. J.* **2018**, *18*, 4022–4029. [CrossRef]

30. Furube, A.; Asahi, T.; Masuhara, H.; Yamashita, H.; Anpo, M. Charge carrier dynamics of standard TiO$_2$ catalysts revealed by femtosecond diffuse reflectance spectroscopy. *J. Phys. Chem. B* **1999**, *103*, 3120–3127. [CrossRef]

31. Ohtani, B.; Ogawa, Y.; Nishimoto, S.-I. Photocatalytic activity of amorphous−anatase mixture of Titanium(IV) oxide particles suspended in aqueous solutions. *J. Phys. Chem. B* **1997**, *101*, 3746–3752. [CrossRef]

32. Stone, V.F.; Davis, R.J. Synthesis, Characterization, and Photocatalytic Activity of Titania and Niobia Mesoporous Molecular Sieves. *Chem. Mater.* **1998**, *10*, 1468–1474. [CrossRef]

33. Tanaka, K.; Capule, M.F.V.; Hisanaga, T. Effect of crystallinity of TiO$_2$ on its photocatalytic action. *Chem. Phys. Lett.* **1991**, *187*, 73–76. [CrossRef]

34. Liu, N.; Albu, S.P.; Lee, K.; So, S.; Schmuki, P. Water annealing and other low temperature treatments of anodic TiO$_2$ nanotubes: A comparison of properties and efficiencies in dye sensitized solar cells and for water splitting. *Electrochim. Acta* **2012**, *82*, 98–102. [CrossRef]

35. Gong, J.; Lai, Y.; Lin, C. Electrochemically multi-anodized TiO$_2$ nanotube arrays for enhancing hydrogen generation by photoelectrocatalytic water splitting. *Electrochim. Acta* **2010**, *55*, 4776–4782. [CrossRef]

36. Tiwari, J.N.; Tiwari, R.N.; Kim, K.S. Zero-dimensional, one-dimensional, two-dimensional and three-dimensional nanostructured materials for advanced electrochemical energy devices. *Prog. Mater. Sci.* **2012**, *57*, 724–803. [CrossRef]

37. Joy, J.; Mathew, J.; George, S.C. Nanomaterials for photoelectrochemical water splitting—Review. *Int. J. Hydrog. Energy* **2018**, *43*, 4804–4817. [CrossRef]

38. Kumar, P.; Devi, P.; Jain, R.; Shivaprasad, S.M.; Sinha, R.K.; Zhou, G.; Nötzel, R. Quantum dot activated indium gallium nitride on silicon as photoanode for solar hydrogen generation. *Commun. Chem.* **2019**, *2*, 4. [CrossRef]

39. Basu, K.; Zhang, H.; Zhao, H.; Bhattacharya, S.; Navarro-Pardo, F.; Datta, P.K.; Jin, L.; Sun, S.; Vetrone, F.; Rosei, F. Highly stable photoelectrochemical cells for hydrogen production using a SnO$_2$–TiO$_2$/quantum dot heterostructured photoanode. *Nanoscale* **2018**, *10*, 15273–15284. [CrossRef] [PubMed]

40. Liu, Z.; Wu, J.; Zhang, J. Quantum dots and plasmonic Ag decorated WO3 nanorod photoanodes with enhanced photoelectrochemical performances. *Int. J. Hydrog. Energy* **2016**, *41*, 20529–20535. [CrossRef]

41. Beermann, N.; Vayssieres, L.; Lindquist, S.E.; Hagfeldt, A. Photoelectrochemical studies of oriented nanorod thin films of hematite. *J. Electrochem. Soc.* **2000**, *147*, 2456–2461. [CrossRef]

42. Khan, S.U.M.; Sultana, T. Photoresponse of n-TiO$_2$ thin film and nanowire electrodes. *Sol. Energy Mat. Sol. Cells* **2003**, *76*, 211–221. [CrossRef]

43. Fitch, A.; Strandwitz, N.C.; Brunschwig, B.S.; Lewis, N.S. A comparison of the behavior of single crystalline and nanowire array ZnO photoanodes. *J. Phys. Chem. C* **2013**, *117*, 2008–2015. [CrossRef]

44. Zhang, J.Z. Metal oxide nanomaterials for solar hydrogen generation from photoelectrochemical water splitting. *Mrs Bull.* **2011**, *36*, 48–55. [CrossRef]

45. Varghese, O.K.; Grimes, C.A. Appropriate strategies for determining the photoconversion efficiency of water photoelectrolysis cells: A review with examples using titania nanotube array photoanodes. *Sol. Energy Mat. Sol. Cells* **2008**, *92*, 374–384. [CrossRef]

46. Huang, H.; Hou, X.; Xiao, J.; Zhao, L.; Huang, Q.; Chen, H.; Li, Y. Effect of annealing atmosphere on the performance of TiO$_2$ nanorod arrays in photoelectrochemical water splitting. *Catal. Today* **2019**, *330*, 189–194. [CrossRef]

47. Nie, Q.; Yang, L.; Cao, C.; Zeng, Y.; Wang, G.; Wang, C.; Lin, S. Interface optimization of ZnO nanorod/CdS quantum dots heterostructure by a facile two-step low-temperature thermal treatment for improved photoelectrochemical water splitting. *Chem. Eng. J.* **2017**, *325*, 151–159. [CrossRef]

48. Pokrant, S.; Dilger, S.; Landsmann, S.; Trottmann, M. Size effects of cocatalysts in photoelectrochemical and photocatalytic water splitting. *Mater. Today Energy* **2017**, *5*, 158–163. [CrossRef]

49. Kudo, A.; Miseki, Y. Heterogeneous photocatalyst materials for water splitting. *Chem. Soc. Rev.* **2009**, *38*, 253–278. [CrossRef] [PubMed]

50. Liu, X.; Gu, S.; Zhao, Y.; Zhou, G.; Li, W. BiVO4, Bi$_2$WO$_6$ and Bi$_2$MoO$_6$ photocatalysis: A brief review. *J. Mater. Sci. Technol.* **2020**, *56*, 45–68. [CrossRef]

51. Vishwakarma, A.K.; Tripathi, P.; Srivastava, A.; Sinha, A.S.K.; Srivastava, O.N. Band gap engineering of Gd and Co doped BiFeO$_3$ and their application in hydrogen production through photoelectrochemical route. *Int. J. Hydrog. Energy* **2017**, *42*, 22677–22686. [CrossRef]

52. Yin, W.-J.; Tang, H.; Wei, S.-H.; Al-Jassim, M.M.; Turner, J.; Yan, Y. Band structure engineering of semiconductors for enhanced photoelectrochemical water splitting: The case of TiO$_2$. *Phys. Rev. B* **2010**, *82*, 045106. [CrossRef]

53. Wang, J.; Sun, H.; Huang, J.; Li, Q.; Yang, J. Band Structure Tuning of TiO$_2$ for Enhanced Photoelectrochemical Water Splitting. *J. Phys. Chem. C* **2014**, *118*, 7451–7457. [CrossRef]

54. Zhang, G.; Zhang, W.; Minakata, D.; Chen, Y.C.; Crittenden, J.; Wang, P. The pH effects on H$_2$ evolution kinetics for visible light water splitting over the Ru/(CuAg)0.15In0.3Zn1.4S2 photocatalyst. *Int. J. Hydrog. Energy* **2013**, *38*, 11727–11736. [CrossRef]

55. Fekete, M.; Riedel, W.; Patti, A.F.; Spiccia, L. Photoelectrochemical water oxidation by screen printed ZnO nanoparticle films: Effect of pH on catalytic activity and stability. *Nanoscale* **2014**, *6*, 7585–7593. [CrossRef]

56. Momeni, M.M.; Ghayeb, Y. Visible light-driven photoelectrochemical water splitting on ZnO–TiO$_2$ heterogeneous nanotube photoanodes. *J. Appl. Electrochem.* **2015**, *45*, 557–566. [CrossRef]

57. Varadhan, P.; Fu, H.-C.; Priante, D.; Retamal, J.R.D.; Zhao, C.; Ebaid, M.; Ng, T.K.; Ajia, I.; Mitra, S.; Roqan, I.S.; et al. Surface Passivation of GaN Nanowires for Enhanced Photoelectrochemical Water-Splitting. *Nano Lett.* **2017**, *17*, 1520–1528. [CrossRef] [PubMed]

58. Ismail, A.A.; Bahnemann, D.W. Photochemical splitting of water for hydrogen production by photocatalysis: A review. *Sol. Energy Mat. Sol. Cells* **2014**, *128*, 85–101. [CrossRef]

59. Kresse, G.; Furthmüller, J. Efficient iterative schemes for ab initio total-energy calculations using a plane-wave basis set. *Phys. Rev. B* **1996**, *54*, 11169–11186. [CrossRef]

60. Kresse, G.; Furthmüller, J. Efficiency of ab-initio total energy calculations for metals and semiconductors using a plane-wave basis set. *Comp. Mater. Sci.* **1996**, *6*, 15–50. [CrossRef]

61. Kresse, G.; Hafner, J. Ab initio molecular dynamics for liquid metals. *Phys. Rev. B* **1993**, *47*, 558–561. [CrossRef]

62. Kresse, G.; Hafner, J. Ab initio molecular-dynamics simulation of the liquid-metal-amorphous-semiconductor transition in germanium. *Phys. Rev. B* **1994**, *49*, 14251–14269. [CrossRef] [PubMed]

63. Kresse, G.; Hafner, J. Norm-conserving and ultrasoft pseudopotentials for first-row and transition elements. *J. Phys.-Condens Mat.* **1994**, *6*, 8245–8257. [CrossRef]

64. Kresse, G.; Joubert, D. From ultrasoft pseudopotentials to the projector augmented-wave method. *Phys. Rev. B* **1999**, *59*, 1758–1775. [CrossRef]

65. Clark, S.J.; Segall, M.D.; Pickard, C.J.; Hasnip, P.J.; Probert, M.I.J.; Refson, K.; Payne, M.C. First principles methods using CASTEP. *Z. Krist.-Cryst. Mater.* **2005**, *220*, 567–570. [CrossRef]

66. Dovesi, R.; Erba, A.; Orlando, R.; Zicovich-Wilson, C.M.; Civalleri, B.; Maschio, L.; Rérat, M.; Casassa, S.; Baima, J.; Salustro, S.; et al. Quantum-mechanical condensed matter simulations with CRYSTAL. *Wires Comput. Mol. Sci.* **2018**, *8*, e1360. [CrossRef]

67. Dovesi, R.; Pascale, F.; Civalleri, B.; Doll, K.; Harrison, N.M.; Bush, I.; D'Arco, P.; Noël, Y.; Rérat, M.; Carbonnière, P.; et al. The CRYSTAL code, 1976–2020 and beyond, a long story. *J. Chem. Phys.* **2020**, *152*, 204111. [CrossRef]

68. Mortensen, J.J.; Hansen, L.B.; Jacobsen, K.W. Real-space grid implementation of the projector augmented wave method. *Phys. Rev. B* **2005**, *71*, 035109. [CrossRef]

69. Kan, M.; Wang, J.Y.; Li, X.W.; Zhang, S.H.; Li, Y.W.; Kawazoe, Y.; Sun, Q.; Jena, P. Structures and Phase Transition of a MoS2 Monolayer. *J. Phys. Chem. C* **2014**, *118*, 1515–1522. [CrossRef]

70. Xia, Z.; Tao, Y.; Pan, Z.; Shen, X. Enhanced photocatalytic performance and stability of 1T MoS2 transformed from 2H MoS2 via Li intercalation. *Results Phys.* **2019**, *12*, 2218–2224. [CrossRef]

71. Liu, P.; Kaltak, M.; Klimeš, J.; Kresse, G. Cubic scaling GW: Towards fast quasiparticle calculations. *Phys. Rev. B* **2016**, *94*, 165109. [CrossRef]

72. Ramberger, B.; Sukurma, Z.; Schäfer, T.; Kresse, G. RPA natural orbitals and their application to post-Hartree-Fock electronic structure methods. *J. Chem. Phys.* **2019**, *151*, 214106. [CrossRef]

73. Heyd, J.; Scuseria, G.E. Efficient hybrid density functional calculations in solids: Assessment of the Heyd-Scuseria-Ernzerhof screened Coulomb hybrid functional. *J. Chem. Phys.* **2004**, *121*, 1187–1192. [CrossRef]

74. Heyd, J.; Scuseria, G.E.; Ernzerhof, M. Hybrid functionals based on a screened Coulomb potential. *J. Chem. Phys.* **2003**, *118*, 8207–8215. [CrossRef]

75. Perdew, J.P.; Burke, K.; Ernzerhof, M. Generalized Gradient Approximation Made Simple. *Phys. Rev. Lett.* **1996**, *77*, 3865–3868. [CrossRef] [PubMed]

76. Wang, V.; Xu, N.; Liu, J.C.; Tang, G.; Geng, W.-T. VASPKIT: A User-friendly Interface Facilitating High-throughput Computing and Analysis Using VASP Code. *arXiv* **2019**, arXiv:1908.08269.

77. Togo, A.; Tanaka, I. First principles phonon calculations in materials science. *Scr. Mater.* **2015**, *108*, 1–5. [CrossRef]

78. Kumar, A. Different methods used for the synthesis of TiO$_2$ based nanomaterials: A review. *Am. J. Nano Res. Appl.* **2018**, *6*, 1. [CrossRef]

79. Nagaraju, G.; Tharamani, C.; Chandrappa, G.; Livage, J. Hydrothermal synthesis of amorphous MoS2nanofiber bundles via acidification of ammonium heptamolybdate tetrahydrate. *Nanoscale Res. Lett.* **2007**, *2*, 461–468. [CrossRef]

80. Bai, J.; Meng, T.; Guo, D.; Wang, S.; Mao, B.; Cao, M. Co9S8@MoS2 Core–Shell Heterostructures as Trifunctional Electrocatalysts for Overall Water Splitting and Zn–Air Batteries. *ACS Appl. Mater. Interfaces* **2018**, *10*, 1678–1689. [CrossRef]

81. Lee, J.-H.; Choi, H.-S.; Lee, J.-H.; Kim, Y.-J.; Suh, S.-J.; Chi, C.-S.; Oh, H.-J. Fabrication of titania nanotubular film with metal nanoparticles. *J. Cryst. Growth* **2009**, *311*, 638–641. [CrossRef]

82. Patil, U.M.; Kulkarni, S.B.; Deshmukh, P.R.; Salunkhe, R.R.; Lokhande, C.D. Photosensitive nanostructured TiO$_2$ grown at room temperature by novel "bottom-up" approached CBD method. *J. Alloy. Compd.* **2011**, *509*, 6196–6199. [CrossRef]

83. Wu, J.-M.; Hayakawa, S.; Tsuru, K.; Osaka, A. Nanocrystalline Titania Made from Interactions of Ti with Hydrogen Peroxide Solutions Containing Tantalum Chloride. *Cryst. Growth Des.* **2002**, *2*, 147–149. [CrossRef]

84. AlHammad, M.S. Nanostructure hydroxyapatite based ceramics by sol gel method. *J. Alloy. Compd.* **2016**, *661*, 251–256. [CrossRef]

85. Kluson, P.; Luskova, H.; Cajthaml, T.; Šolcová, O. Non thermal preparation of photoactive titanium (IV) oxide thin layers. *Thin Solid Film.* **2006**, *495*, 18–23. [CrossRef]

86. Arami, H.; Mazloumi, M.; Khalifehzadeh, R.; Sadrnezhaad, S.K. Sonochemical preparation of TiO$_2$ nanoparticles. *Mater. Lett.* **2007**, *61*, 4559–4561. [CrossRef]

87. Amaresh, S.; Karthikeyan, K.; Jang, I.C.; Lee, Y.S. Single-step microwave mediated synthesis of the CoS2 anode material for high rate hybrid supercapacitors. *J. Mater. Chem. A* **2014**, *2*, 11099–11106. [CrossRef]

88. Pan, Y.; Wen, M. Noble metals enhanced catalytic activity of anatase TiO$_2$ for hydrogen evolution reaction. *Int. J. Hydrog. Energy* **2018**, *43*, 22055–22063. [CrossRef]

89. Zhang, Y.; Kilin, D.S. Computational modeling of wet TiO2(001) anatase surfaces functionalized by transition metal doping. *Int. J. Quantum Chem.* **2012**, *112*, 3867–3873. [CrossRef]

90. Zhang, S.-T.; Li, C.-M.; Yan, H.; Wei, M.; Evans, D.G.; Duan, X. Density Functional Theory Study on the Metal–Support Interaction between Ru Cluster and Anatase TiO$_2$(101) Surface. *J. Phys. Chem. C* **2014**, *118*, 3514–3522. [CrossRef]

91. Jin, C.; Dai, Y.; Wei, W.; Ma, X.; Li, M.; Huang, B. Effects of single metal atom (Pt, Pd, Rh and Ru) adsorption on the photocatalytic properties of anatase TiO$_2$. *Appl. Surf. Sci.* **2017**, *426*, 639–646. [CrossRef]

92. Lin, Y.; Jiang, Z.; Zhu, C.; Zhang, R.; Hu, X.; Zhang, X.; Zhu, H.; Lin, S.H. The electronic structure, optical absorption and photocatalytic water splitting of (Fe + Ni)-codoped TiO$_2$: A DFT + U study. *Int. J. Hydrog. Energy* **2017**, *42*, 4966–4976. [CrossRef]

93. Ghuman, K.K. Mechanistic insights into water adsorption and dissociation on amorphous -based catalysts. *Sci. Technol. Adv. Mater.* **2018**, *19*, 44–52. [CrossRef]

94. Koteski, V.; Belošević-Čavor, J.; Umićević, A.; Ivanovski, V.; Toprek, D. Improving the photocatalytic properties of anatase TiO$_2$(101) surface by co-doping with Cu and N: Ab initio study. *Appl. Surf. Sci.* **2017**, *425*, 1095–1100. [CrossRef]

95. Assadi, M.H.N.; Hanaor, D.A.H. The effects of copper doping on photocatalytic activity at (101) planes of anatase TiO$_2$: A theoretical study. *Appl. Surf. Sci.* **2016**, *387*, 682–689. [CrossRef]

96. Sikam, P.; Moontragoon, P.; Sararat, C.; Karaphun, A.; Swatsitang, E.; Pinitsoontorn, S.; Thongbai, P. DFT calculation and experimental study on structural, optical and magnetic properties of Co-doped SrTiO$_3$. *Appl. Surf. Sci.* **2018**, *446*, 92–113. [CrossRef]

97. Ghuman, K.K.; Singh, C.V. Effect of doping on electronic structure and photocatalytic behavior of amorphous TiO$_2$. *J. Phys.-Condens Mat.* **2013**, *25*, 475501. [CrossRef]

98. Ren, D.; Li, H.; Cheng, X. Tailoring the electronic and optical properties of anatase TiO$_2$ by (S, Nb) co-doping from a DFT plus U calculation. *Solid State Commun.* **2015**, *223*, 54–59. [CrossRef]

99. Gao, L.; Li, Y.; Ren, J.; Wang, S.; Wang, R.; Fu, G.; Hu, Y. Passivation of defect states in anatase TiO$_2$ hollow spheres with Mg doping: Realizing efficient photocatalytic overall water splitting. *Appl. Catal. B-Environ.* **2017**, *202*, 127–133. [CrossRef]

100. Chen, W.; Yuan, P.; Zhang, S.; Sun, Q.; Liang, E.; Jia, Y. Electronic properties of anatase TiO$_2$ doped by lanthanides: A DFT+U study. *Phys. B* **2012**, *407*, 1038–1043. [CrossRef]

101. Li, H.; Li, W.; Liu, X.; Ren, C.; Miao, X.; Li, X. Engineering of Gd/Er/Lu-triple-doped Bi2MoO6 to synergistically boost the photocatalytic performance in three different aspects: Oxidizability, light absorption and charge separation. *Appl. Surf. Sci.* **2019**, *463*, 556–565. [CrossRef]

102. Shi, H.; Lin, Y.; Jiang, Z.; Su, Y.; Ding, X.; Zhang, X.; Zhu, H.; Zhang, R. Enhanced optical absorption and photocatalytic activity of anatase TiO$_2$ through C Nd-codoped: A DFT+ U calculations. *J. Phys. Chem. Solids* **2017**, *109*, 70–77. [CrossRef]

103. Jiang, Z.; Wan, W.; Wei, W.; Chen, K.; Li, H.; Wong, P.K.; Xie, J. Gentle way to build reduced titanium dioxide nanodots integrated with graphite-like carbon spheres: From DFT calculation to experimental measurement. *Appl. Catal. B-Environ.* **2017**, *204*, 283–295. [CrossRef]

104. Gurkan, Y.Y.; Kasapbasi, E.; Cinar, Z. Enhanced solar photocatalytic activity of TiO$_2$ by selenium(IV) ion-doping: Characterization and DFT modeling of the surface. *Chem. Eng. J.* **2013**, *214*, 34–44. [CrossRef]

105. Zhao, Y.; Wang, W.; He, L. The effects of Co/N dopants on the electronic, redox potential, optical, and photocatalytic water-splitting properties of TiO$_2$: First principles calculations. *Chem. Phys. Lett.* **2017**, *685*, 108–113. [CrossRef]

106. Wang, P.; Zhou, Q.; Xia, Y.; Zhan, S.; Li, Y. Understanding the charge separation and transfer in mesoporous carbonate-doped phase-junction TiO$_2$ nanotubes for photocatalytic hydrogen production. *Appl. Catal. B-Environ.* **2018**, *225*, 433–444. [CrossRef]

107. Wu, X.; Yin, S.; Dong, Q.; Guo, C.; Kimura, T.; Matsushita, J.-I.; Sato, T. Photocatalytic properties of Nd and C Codoped TiO$_2$ with the whole range of visible light absorption. *J. Phys. Chem. C* **2013**, *117*, 8345–8352. [CrossRef]

108. Zongyan, Z.; Xiang, Z.; Juan, Y.; Qingju, L. Effects of nonmetal doping on electronic structures and optical property of anatase TiO$_2$ from first-principles calculations. *Rare Met. Mat. Eng.* **2015**, *44*, 1568–1574. [CrossRef]

109. Zhao, Y.; Lin, Y.; Wang, G.; Jiang, Z.; Zhang, R.; Zhu, C. Electronic and optical performances of (Cu, N) codoped TiO$_2$/g-C3N4 heterostructure photocatalyst: A spin-polarized DFT + U study. *Sol. Energy* **2018**, *162*, 306–316. [CrossRef]

110. Lin, Y.; Shi, H.; Jiang, Z.; Wang, G.; Zhang, X.; Zhu, H.; Zhang, R.; Zhu, C. Enhanced optical absorption and photocatalytic H$_2$ production activity of g-C3N4/TiO$_2$ heterostructure by interfacial coupling: A DFT+ U study. *Int. J. Hydrog. Energy* **2017**, *42*, 9903–9913. [CrossRef]

111. Atanelov, J.; Gruber, C.; Mohn, P. The electronic and magnetic structure of p -element (C,N) doped rutile-TiO$_2$: A hybrid DFT study. *Comput. Mater. Sci.* **2015**, *98*, 42–50. [CrossRef]

112. Ghuman, K.K.; Singh, C.V. A DFT + U study of (Rh, Nb)-codoped rutile TiO$_2$. *J. Phys.-Condens Mat.* **2013**, *25*, 085501. [CrossRef]

113. Lisovski, O.; Chesnokov, A.; Piskunov, S.; Bocharov, D.; Zhukovskii, Y.F.; Wessel, M.; Spohr, E. Ab initio calculations of doped TiO$_2$ anatase (101) nanotubes for photocatalytical water splitting applications. *Mat. Sci. Semicon. Proc* **2016**, *42*, 138–141. [CrossRef]

114. Lisovski, O.; Piskunov, S.; Zhukovskii, Y.F.; Ozolins, J. Ab initiomodeling of sulphur doped TiO$_2$ nanotubular photocatalyst for water-splitting hydrogen generation. *Iop Conf. Ser.-Mat. Sci.* **2012**, *38*. [CrossRef]

115. Bocharov, D.; Piskunov, S.; Zhukovskii, Y.F.; Spohr, E.; D'Yachkov, P.N. First principles modeling of 3 d -metal doped three-layer fluorite-structured TiO$_2$(4,4) nanotube to be used for photocatalytic hydrogen production. *Vacuum* **2017**, *146*, 562–569. [CrossRef]

116. D'yachkov, E.P.; Bochkov, I.A.; Zaluev, V.A.; D'yachkova, P.N. Electronic properties of titanium dioxide nanotubes doped with 4d metals. *Russ. J. Inorg. Chem.* **2017**, *62*, 1048–1050. [CrossRef]

117. Lisovski, O.; Piskunov, S.; Zhukovskii, Y.F.; Bocharov, D. Quantum chemical simulations of titanium dioxide nanotubes used for photocatalytic water splitting. *J. Surf. Investig.* **2017**, *11*, 78–86. [CrossRef]

118. Ma, S.; Song, W.; Liu, B.; Zhong, W.; Deng, J.; Zheng, H.; Liu, J.; Gong, X.-Q.; Zhao, Z. Facet-dependent photocatalytic performance of TiO$_2$: A DFT study. *Appl. Catal. B-Environ.* **2016**, *198*, 1–8. [CrossRef]

119. Deák, P.; Kullgren, J.; Aradi, B.; Frauenheim, T.; Kavan, L. Water splitting and the band edge positions of TiO$_2$. *Electrochim. Acta* **2016**, *199*, 27–34. [CrossRef]

120. Hanaor, D.A.H.; Assadi, M.H.N.; Li, S.; Yu, A.; Sorrel, C.C. Ab Initio Study of Phase Stability in Doped TiO$_2$. *Comput. Mech.* **2012**, *50*, 185–194. [CrossRef]

121. Alghamdi, H.; Idriss, H. Study of the modes of adsorption and electronic structure of hydrogen peroxide and ethanol over TiO$_2$ rutile (110) surface within the context of water splitting. *Surf. Sci.* **2017**. [CrossRef]

122. Tsai, C.; Chan, K.; Nørskov, J.K.; Abild-Pedersen, F. Theoretical insights into the hydrogen evolution activity of layered transition metal dichalcogenides. *Surf. Sci.* **2015**, *640*, 133–140. [CrossRef]

123. Li, Z.; Shi, L.; Franklin, D.; Koul, S.; Kushima, A.; Yang, Y. Drastic enhancement of photoelectrochemical water splitting performance over plasmonic Al@TiO2 heterostructured nanocavity arrays. *Nano Energy* **2018**, *51*, 400–407. [CrossRef]

124. Venturini, J.; Bonatto, F.; Guaglianoni, W.C.; Lemes, T.; Arcaro, S.; Alves, A.K.; Bergmann, C.P. Cobalt-doped titanium oxide nanotubes grown via one-step anodization for water splitting applications. *Appl. Surf. Sci.* **2019**, *464*, 351–359. [CrossRef]

125. Dong, Z.; Ding, D.; Li, T.; Ning, C. Ni-doped TiO$_2$ nanotubes photoanode for enhanced photoelectrochemical water splitting. *Appl. Surf. Sci.* **2018**, *443*, 321–328. [CrossRef]

126. Li, Y.; Wang, J.-G.; Fan, Y.; Sun, H.; Hua, W.; Liu, H.; Wei, B. Plasmonic TiN boosting nitrogen-doped TiO$_2$ for ultrahigh efficient photoelectrochemical oxygen evolution. *Appl. Catal. B-Environ.* **2019**, *246*, 21–29. [CrossRef]

127. Park, J.; Desmukh, P.R.; Sohn, y.; Shin, W.G. ZnO-TiO$_2$ core-shell nanowires decorated with Au nanoparticles for plasmon-enhanced photoelectrochemical water splitting. *J. Alloy. Compd.* **2019**, *787*, 1310–1319. [CrossRef]

128. Zhang, S.; Cao, X.-b.; Wu, J.; Zhu, L.-w.; Gu, L. Preparation of hierarchical CuO@TiO$_2$ nanowire film and its application in photoelectrochemical water splitting. *T. Nonferr. Metal. Soc.* **2016**, *26*, 2094–2101. [CrossRef]

129. Sawant, S.Y.; Sayed, M.S.; Han, T.H.; Karim, M.R.; Shim, J.J.; Cho, M.H. Bio-synthesis of finely distributed Ag nanoparticle-decorated TiO$_2$ nanorods for sunlight-induced photoelectrochemical water splitting. *J. Ind. Eng. Chem.* **2019**, *69*, 48–56. [CrossRef]

130. Liu, J.; Ke, J.; Li, Y.; Liu, B.J.; Wang, L.D.; Xiao, H.N.; Wang, S.B. Co3O4 quantum dots/TiO$_2$ nanobelt hybrids for highly efficient photocatalytic overall water splitting. *Appl. Catal. B-Environ.* **2018**, *236*, 396–403. [CrossRef]

131. He, J.; Wang, M.; Wu, X.; Sun, Y.; Huang, K.; Chen, H.; Gao, L.; Feng, S. Influence of controlled Pd nanoparticles decorated TiO$_2$ nanowire arrays for efficient photoelectrochemical water splitting. *J. Alloy. Compd.* **2019**, *785*, 391–397. [CrossRef]

132. Wang, L.; Cao, S.; Guo, K.; Wu, Z.; Ma, Z.; Piao, L. Simultaneous hydrogen and peroxide production by photocatalytic water splitting. *Chin. J. Catal.* **2019**, *40*, 470–475. [CrossRef]

133. Hussain, E.; Majeed, I.; Nadeem, M.A.; Iqbal, A.; Chen, Y.; Choucair, M.; Jin, R.; Nadeem, M.A. Remarkable effect of BaO on photocatalytic H$_2$ evolution from water splitting via TiO$_2$ (P25) supported palladium nanoparticles. *J. Environ. Chem. Eng.* **2019**, *7*, 102729. [CrossRef]

134. Yoo, I.-H.; Kalanur, S.S.; Seo, H. A nanoscale p–n junction photoelectrode consisting of an NiOx layer on a TiO$_2$/CdS nanorod core-shell structure for highly efficient solar water splitting. *Appl. Catal. B-Environ.* **2019**, *250*, 200–212. [CrossRef]

135. Wang, Z.W.; Li, X.L.; Tan, C.K.; Qian, C.; Grimsdale, A.C.; Tok, A.I.Y. Highly porous SnO$_2$ nanosheet arrays sandwiched within TiO$_2$ and CdS quantum dots for efficient photoelectrochemical water splitting. *Appl. Surf. Sci.* **2019**, *470*, 800–806. [CrossRef]

136. Dong, Z.; Ding, D.; Li, T.; Ning, C. Facile preparation of Ti^{3+}/Ni co-doped TiO$_2$ nanotubes photoanode for efficient photoelectro-chemical water splitting. *Appl. Surf. Sci.* **2019**, *480*, 219–228. [CrossRef]

137. Hu, M.; Xing, Z.; Cao, Y.; Li, Z.; Yan, X.; Xiu, Z.; Zhao, T.; Yang, S.; Zhou, W. Ti3+ self-doped mesoporous black TiO$_2$/SiO$_2$/g-C3N4 sheets heterojunctions as remarkable visible-lightdriven photocatalysts. *Appl. Catal. B-Environ.* **2018**, *226*, 499–508. [CrossRef]

138. Wu, L.L.; Shi, S.; Li, Q.D.; Zhang, X.Y.; Cui, X.L. TiO$_2$ nanoparticles modified with 2D MoSe2 for enhanced photocatalytic activity on hydrogen evolution. *Int. J. Hydrog. Energy* **2019**, *44*, 720–728. [CrossRef]

139. Zhang, H.W.; Ma, L.; Ming, J.T.; Liu, B.Q.; Zhao, Y.B.; Hou, Y.D.; Ding, Z.X.; Xu, C.; Zhang, Z.Z.; Long, J.L. Amorphous Ta2OxNy-enwrapped TiO$_2$ rutile nanorods for enhanced solar photoelectrochemical water splitting. *Appl. Catal. B-Environ.* **2019**, *243*, 481–489. [CrossRef]

140. Kaur, G.; Pandey, O.P.; Singh, K. Optical, structural, and mechanical properties of different valence-cation-doped bismuth vanadate oxides. *Phys. Status Solidi A* **2012**, *209*, 1231–1238. [CrossRef]

141. Yang, S.Y.; Seidel, J.; Byrnes, S.J.; Shafer, P.; Yang, C.H.; Rossell, M.D.; Yu, P.; Chu, Y.H.; Scott, J.F.; Ager Iii, J.W.; et al. Above-bandgap voltages from ferroelectric photovoltaic devices. *Nat. Nanotechnol.* **2010**, *5*, 143. [CrossRef]

142. Kay, A.; Cesar, I.; Grätzel, M. New Benchmark for Water Photooxidation by Nanostructured α-Fe$_2$O$_3$ Films. *J. Am. Chem. Soc.* **2006**, *128*, 15714–15721. [CrossRef] [PubMed]

143. Wu, X.; Li, H.; Wang, X.; Jiang, L.; Xi, J.; Du, G.; Ji, Z. Ferroelectric enhanced photoelectrochemical water splitting in BiFeO$_3$/TiO$_2$ composite photoanode. *J. Alloy. Compd.* **2019**, *783*, 643–651. [CrossRef]

144. Jia, Y.L.; Wang, Z.H.; Ma, Y.; Liu, J.L.; Shi, W.B.; Lin, Y.H.; Hu, X.; Zhang, K. Boosting interfacial charge migration of TiO$_2$/BiVO$_4$ photoanode by W doping for photoelectrochemical water splitting. *Electrochim. Acta.* **2019**, *300*, 138–144. [CrossRef]

145. Zhou, W.F.; Jiang, T.F.; Zhao, Y.; Xu, C.; Pei, C.G.; Xue, H.G. Ultrathin Ti/TiO$_2$/BiVO$_4$ nanosheet heterojunction arrays for photoelectrochemical water oxidation. *J. Alloy. Compd.* **2019**, *777*, 1152–1158. [CrossRef]

146. Liu, Q.; Mo, R.; Li, X.L.; Yang, S.; Zhong, J.X.; Li, H.X. Cobalt phosphate modified 3D TiO$_2$/BiVO$_4$ composite inverse opals photoanode for enhanced photoelectrochemical water splitting. *Appl. Surf. Sci.* **2019**, *464*, 544–551. [CrossRef]

147. Yin, X.; Liu, Q.; Yang, Y.H.; Liu, Y.; Wang, K.K.; Li, Y.M.; Li, D.W.; Qiu, X.Q.; Li, W.Z.; Li, J. An efficient tandem photoelectrochemical cell composed of FeOOH/TiO$_2$/BiVO$_4$ and Cu$_2$O for self-driven solar water splitting. *Int. J. Hydrog. Energy* **2019**, *44*, 594–604. [CrossRef]

148. Polo, A.; Grigioni, I.; Dozzi, M.V.; Selli, E. Sensitizing effects of BiVO4 and visible light induced production of highly reductive electrons in the TiO$_2$/BiVO$_4$ heterojunction. *Catal. Today* **2018**. [CrossRef]

149. Radzi, A.A.S.M.; Safaei, J.; Teridi, M.A.M. Photoelectrochemical enhancement from deposition of BiVO4 photosensitizer on different thickness layer TiO$_2$ photoanode for water splitting application. *Nano-Struct. Nano-Objects* **2019**, *18*. [CrossRef]

150. Chai, X.B.; Zhang, H.F.; Pan, Q.; Bian, J.L.; Chen, Z.F.; Cheng, C.W. 3D ordered urchin-like TiO$_2$@Fe$_2$O$_3$ arrays photoanode for efficient photoelectrochemical water splitting. *Appl. Surf. Sci.* **2019**, *470*, 668–676. [CrossRef]

151. Zhang, W.; Chen, H.; Zhang, L.; Zhang, P.; Dong, E.; Ma, J.; Wang, G. Design and fabrication of an α-Fe$_2$O$_3$ TiO$_2$ Si 3D hierarchical photoanode for improved photoelectrochemical water splitting. *J. Alloy. Compd.* **2019**, *773*, 597–604. [CrossRef]

152. Feng, F.; Li, C.; Jian, J.; Qiao, X.; Wang, H.; Jia, L. Boosting hematite photoelectrochemical water splitting by decoration of TiO2 at the grain boundaries. *Chem. Eng. J.* **2019**, *368*, 959–967. [CrossRef]

153. Deng, J.; Zhuo, Q.; Lv, X. Hierarchical TiO2 Fe2O3 heterojunction photoanode for improved photoelectrochemical water oxidation. *J. Electroanal. Chem.* **2019**, *835*, 287–292. [CrossRef]

154. Yoon, J.W.; Kim, D.H.; Kim, J.H.; Jang, H.W.; Lee, J.H. NH2-MIL-125(Ti)/TiO$_2$ nanorod heterojunction photoanodes for efficient photoelectrochemical water splitting. *Appl. Catal. B-Environ.* **2019**, *244*, 511–518. [CrossRef]

155. Yalçın, Y.; Kılıç, M.; Çınar, Z. The Role of Non-Metal Doping in TiO$_2$ Photocatalysis. *J. Adv. Oxid. Technol.* **2010**, *13*, 281. [CrossRef]

156. Lu, Y.; Wei, Z.; Salke, N.P.; Yu, L.; Yan, H. Enhanced electron transport in rutile TiO$_2$ nanowires via H2S-assisted incorporation of dissolved silicon for solar-driven water splitting. *Appl. Catal. B-Environ.* **2019**, *244*, 767–772. [CrossRef]

157. Bayat, A.; Saievar-Iranizad, E. Graphene quantum dots decorated rutile TiO$_2$ nanoflowers for water splitting application. *J. Energy Chem.* **2018**, *27*, 306–310. [CrossRef]

158. Bellamkonda, S.; Thangavel, N.; Hafeez, H.Y.; Neppolian, B.; Rao, G.R. Highly active and stable multi-walled carbon nanotubes-graphene-TiO$_2$ nanohybrid: An efficient non-noble metal photocatalyst for water splitting. *Catal. Today* **2019**, *321*, 120–127. [CrossRef]

159. Gao, Q.; Si, F.; Zhang, S.; Fang, Y.; Chen, X.; Yang, S. Hydrogenated F-doped TiO$_2$ for photocatalytic hydrogen evolution and pollutant degradation. *Int. J. Hydrog. Energy* **2019**, *44*, 8011–8019. [CrossRef]

160. Elbakkay, M.H.; El Rouby, W.M.A.; El-Dek, S.I.; Farghali, A.A. S-TiO$_2$/S-reduced graphene oxide for enhanced photoelectrochemical water splitting. *Appl. Surf. Sci.* **2018**, *439*, 1088–1102. [CrossRef]

161. Dubnova, L.; Zvolska, M.; Edelmannova, M.; Matejova, L.; Reli, M.; Drobna, H.; Kustrowski, P.; Koci, K.; Capek, L. Photocatalytic decomposition of methanol-water solution over N-La/TiO$_2$ photocatalysts. *Appl. Surf. Sci.* **2019**, *469*, 879–886. [CrossRef]

162. Liu, X.; Cao, X.E.; Liu, Y.; Li, X.; Wang, M.; Li, M. Branched multiphase TiO2 with enhanced photoelectrochemical water splitting activity. *Int. J. Hydrog. Energy* **2018**, *43*, 21365–21373. [CrossRef]

163. Xu, Y.; Ahemd, R.; Klein, D.; Cap, S.; Freedy, K.; McDonnel, S.; Zangari, G. Improving photo-oxidation activity of water by introducing Ti3+ in self-ordered TiO$_2$ nanotube arrays treated with Ar NH3. *J. Power Sour.* **2019**, *414*, 242–249. [CrossRef]

164. Xu, Y.; Lin, Q.Y.; Ahmed, R.; Hoglund, E.R.; Zangari, G. Synthesis of TiO$_2$-based nanocomposites by anodizing and hydrogen annealing for efficient photoelectrochemical water oxidation. *J. Power Sour.* **2019**, *410*, 59–68. [CrossRef]

165. Wei, N.; Liu, Y.; Feng, M.; Li, Z.X.; Chen, S.G.; Zheng, Y.B.; Wang, D.A. Controllable TiO$_2$ core-shell phase heterojunction for efficient photoelectrochemical water splitting under solar light. *Appl. Catal. B-Environ.* **2019**, *244*, 519–528. [CrossRef]

166. Alexander, F.; AlMheiri, M.; Dahal, P.; Abed, J.; Rajput, N.S.; Aubry, C.; Viegas, J.; Jouiad, M. Water splitting TiO$_2$ composite material based on black silicon as an efficient photocatalyst. *Sol. Energy Mat. Sol. Cells* **2018**, *180*, 236–242. [CrossRef]

167. Fu, B.; Wu, Z.; Cao, S.; Guo, K.; Piao, L. Effect of aspect ratios of rutile TiO2 nanorods on overall photocatalytic water splitting performance. *Nanoscale* **2020**, *12*, 4895–4902. [CrossRef] [PubMed]

168. Abed, J.; AlMheiri, M.; Alexander, F.; Rajput, N.S.; Viegas, J.; Jouiad, M. Enhanced solar absorption of gold plasmon assisted TiO2-based water splitting composite. *Sol. Energy Mat. Sol. Cells* **2018**, *180*, 228–235. [CrossRef]

169. Pérez-Larios, A.; Lopez, R.; Hernández-Gordillo, A.; Tzompantzi, F.; Gómez, R.; Torres-Guerra, L.M. Improved hydrogen production from water splitting using TiO$_2$–ZnO mixed oxides photocatalysts. *Fuel* **2012**, *100*, 139–143. [CrossRef]

170. Wang, Q.; Huang, J.; Sun, H.; Zhang, K.-Q.; Lai, Y. Uniform carbon dots@TiO2 nanotube arrays with full spectrum wavelength light activation for efficient dye degradation and overall water splitting. *Nanoscale* **2017**, *9*, 16046–16058. [CrossRef] [PubMed]

171. Leung, D.Y.; Fu, X.; Wang, C.; Ni, M.; Leung, M.K.; Wang, X.; Fu, X. Hydrogen production over titania-based photocatalysts. *ChemSusChem* **2010**, *3*, 681–694. [CrossRef]

172. Makhlouf, A.S.H.; Tiginyanu, I. *Nanocoatings and Ultra-Thin Films*; Woodhead Publishing: Cambridge, UK, 2011; p. 448.

173. Hernández-Alonso, M.; Fresno, F.; Suárez, S.; Coronado, J. Development of alternative photocatalysts to TiO$_2$: Challenges and opportunities. *Energy Environ. Sci.* **2009**, *2*, 1231–1257. [CrossRef]

174. Goto, Y.; Hisatomi, T.; Wang, Q.; Higashi, T.; Ishikiriyama, K.; Maeda, T.; Sakata, Y.; Okunaka, S.; Tokudome, H.; Katayama, M.; et al. A Particulate Photocatalyst Water-Splitting Panel for Large-Scale Solar Hydrogen Generation. *Joule* **2018**, *2*, 509–520. [CrossRef]

175. Pinaud, B.A.; Benck, J.D.; Seitz, L.C.; Forman, A.J.; Chen, Z.; Deutsch, T.G.; James, B.D.; Baum, K.N.; Baum, G.N.; Ardo, S.; et al. Technical and economic feasibility of centralized facilities for solar hydrogen production via photocatalysis and photoelectrochemistry. *Energy Environ. Sci.* **2013**, *6*, 1983–2002. [CrossRef]

176. Han, L.; Lin, M.; Haussener, S. Reliable Performance Characterization of Mediated Photocatalytic Water-Splitting Half Reactions. *ChemSusChem* **2017**, *10*, 2158–2166. [CrossRef]

177. Kisch, H.; Bahnemann, D. Best Practice in Photocatalysis: Comparing Rates or Apparent Quantum Yields? *J. Phys. Chem. Lett.* **2015**, *6*, 1907–1910. [CrossRef] [PubMed]

178. Liang, Z.; Zhong, X.; Li, T.; Chen, M.; Feng, G. DFT Study on the Hydrogen Evolution Reaction for Different Facets of Co2P. *ChemElectroChem* **2019**, *6*, 260–267. [CrossRef]

179. Skúlason, E.; Karlberg, G.S.; Rossmeisl, J.; Bligaard, T.; Greeley, J.; Jónsson, H.; Nørskov, J.K. Density functional theory calculations for the hydrogen evolution reaction in an electrochemical double layer on the Pt(111) electrode. *Phys. Chem. Chem. Phys.* **2007**, *9*, 3241–3250. [CrossRef] [PubMed]

180. Parzinger, E.; Miller, B.; Blaschke, B.; Garrido, J.A.; Ager, J.W.; Holleitner, A.; Wurstbauer, U. Photocatalytic Stability of Single- and Few-Layer MoS2. *ACS Nano* **2015**, *9*, 11302–11309. [CrossRef]

181. Li, Z.; Meng, X.; Zhang, Z. Recent development on MoS2-based photocatalysis: A review. *J. Photoch. Photobio. C* **2018**, *35*, 39–55. [CrossRef]

182. Zhao, Y.; Ding, C.; Zhu, J.; Qin, W.; Tao, X.; Fan, F.; Li, R.; Li, C. A Hydrogen Farm Strategy for Scalable Solar Hydrogen Production with Particulate Photocatalysts. *Angew. Chem. Int. Edit.* **2020**, *59*, 9653–9658. [CrossRef] [PubMed]